Cellular and Molecular Life Sciences (2022) 79:553
https://doi.org/10.1007/s00018-022-04587-6

ORIGINAL ARTICLE

A plant-based mutant huntingtin model-driven discovery of impaired expression of GTPCH and DHFR

Chiu-Yueh Hung[1] · Chuanshu Zhu[1,2] · Farooqahmed S. Kittur[1] · Maotao He[1,3] · Erland Arning[4] · Jianhui Zhang[1] · Asia J. Johnson[1] · Gurpreet S. Jawa[1,5] · Michelle D. Thomas[1,6] · Tomas T. Ding[1] · Jiahua Xie[1]

Received: 2 June 2022 / Revised: 13 September 2022 / Accepted: 3 October 2022

Abstract

Pathophysiology associated with Huntington's disease (HD) has been studied extensively in various cell and animal models since the 1993 discovery of the mutant huntingtin (mHtt) with abnormally expanded polyglutamine (polyQ) tracts as the causative factor. However, the sequence of early pathophysiological events leading to HD still remains elusive. To gain new insights into the early polyQ-induced pathogenic events, we expressed Htt exon1 (Htt_{ex1}) with a normal (21), or an extended (42 or 63) number of polyQ in tobacco plants. Here, we show that transgenic plants accumulated Htt_{ex1} proteins with corresponding polyQ tracts, and $mHtt_{ex1}$ induced protein aggregation and affected plant growth, especially root and root hair development, in a polyQ length-dependent manner. Quantitative proteomic analysis of young roots from severely affected Htt_{ex1}Q63 and unaffected Htt_{ex1}Q21 plants showed that the most reduced protein by polyQ63 is a GTP cyclohydrolase I (GTPCH) along with many of its related one-carbon (C_1) metabolic pathway enzymes. GTPCH is a key enzyme involved in folate biosynthesis in plants and tetrahydrobiopterin (BH_4) biosynthesis in mammals. Validating studies in 4-week-old R6/2 HD mice expressing a $mHtt_{ex1}$ showed reduced levels of GTPCH and dihydrofolate reductase (DHFR, a key folate utilization/alternate BH_4 biosynthesis enzyme), and impaired C_1 and BH_4 metabolism. Our findings from $mHtt_{ex1}$ plants and mice reveal impaired expressions of GTPCH and DHFR and may contribute to a better understanding of mHtt-altered C_1 and BH_4 metabolism, and their roles in the pathogenesis of HD.

Keywords Dihydrofolate reductase · GTP cyclohydrolase I · Huntington's disease · One-carbon metabolism · Protein aggregation · Quantitative proteomic analysis · Tetrahydrobiopterin biosynthesis

Introduction

Huntington's disease (HD) and at least eight other polyglutamine (polyQ)-mediated neurodegenerative diseases (NDDs) share the common features of pathological protein aggregation, and age-dependent progressive neurodegeneration [1, 2]. After years of intensive research following the discovery of abnormally expanded polyQ (> 36Q) in huntingtin exon 1 (Htt_{ex1}) as the cause for HD [3], mutant Htt (mHtt) protein was found to alter the protein structure and properties and cause the protein aggregation leading to the dysregulation of many cellular processes, such as gene transcription, proteostasis, mitochondrial function and

Chiu-Yueh Hung, Chuanshu Zhu, Farooqahmed S. Kittur, Maotao He and Erland Arning contributed equally to this work.

✉ Tomas T. Ding
tding@nccu.edu

✉ Jiahua Xie
jxie@nccu.edu

[1] Department of Pharmaceutical Sciences, Biomanufacturing Research Institute and Technology Enterprise, North Carolina Central University, Durham, NC 27707, USA

[2] College of Plant Protection, Northwest A&F University, Yangling, Shaanxi 712100, China

[3] Department of Pathology, Weifang Medical University, Weifang, Shandong 261000, China

[4] Baylor Scott and White Research Institute, Institute of Metabolic Disease, Dallas, TX 75204, USA

[5] Present Address: DePuy Synthes Companies of Johnson & Johnson, West Chester, PA 19380, USA

[6] Present Address: University of North Carolina, Eshelman School of Pharmacy, Chapel Hill, NC 27599, USA

Published online: 17 October 2022

chromatin modification, resulting in cortico-striatal miscommunication and progressive neuronal loss [1, 4–6]. However, the underlying pathophysiological mechanisms are still not fully understood and no effective cure is available [4–6]. Limited study to unravel early cellular events affected by polyQ repeats may be one of the key obstacles to understand the initiation and progression of the disease. Exploring novel systems might facilitate our understanding of disease initiation and progression processes.

Plants could be useful for studying polyQ repeat-induced pathology because both plant and animal cells are eukaryotic and share many similarities; plants however have some unique characteristics. Most importantly, plants naturally lack Htt homologs, and transgenic plants expressing Htt or mHtt would avoid any endogenous Htt's effects, which will simplify the interpretation of polyQ effects compared to any HD animal models. Furthermore, recent molecular, biochemical and physiological studies have shown that plant root apices possess sensing functions, such as receiving, integrating and responding to signals from their environment, and that root hairs share several morphological and biochemical features with neurons, such as a single tubular-shaped cell, long extension tip growth, high energy demand, cell polarity, action potential, and environmental sensing capacity [7, 8]. Therefore, roots and root hairs might be more susceptible to polyQ-induced toxicity than other organs/cells to exhibit phenotypic changes. In addition, plants also possess numerous experimental advantages, such as less ethical requirements, easy cell culture and transformation, and simple growth and seed maintenance. Plants have been utilized to study human diseases in the previous studies [9, 10].

To explore the use of transgenic plants as a system to investigate the toxicity of abnormal polyQ repeats and early affected cellular processes, we first proved that expressing human Htt_{ex1} with different "CAG" repeats in transgenic tobacco (*Nicotiana tabacum*) plants could accumulate Htt_{ex1} with the corresponding polyQ tracts. We then discovered that the toxicity of the expanded polyQ repeats to plant cells was dependent on the repeat length. The most intriguing observation was that polyQ63 inhibited root growth and root hair outgrowth while polyQ21 did not display these inhibitory outcomes. Quantitative proteomic analysis of young adventitious roots induced from shoots of Htt_{ex1}Q63 and Htt_{ex1}Q21 revealed that many differentially abundant proteins (DAPs), which have previously been implicated in HD models, were enriched in various cellular pathways. Most importantly, we discovered that GTP cyclohydrolase I (GTPCH), the rate-limiting enzyme catalyzing the first step in the de novo folate biosynthesis, was the protein most affected by polyQ63. Moreover, we also observed many other DAPs that are involved in activating and transferring one carbon (C_1) units to the various methylation pathways [11, 12]. Previous studies have suggested a possible link between NDDs, including HD, and the disorder of folate-mediated C_1 metabolism [13–16], but the molecular link connecting C_1 metabolism to NDDs has yet to be found. Our findings of polyQ63 impaired GTPCH and its associated C_1 metabolism could be an $mHtt_{ex1}$-induced early event and provide a link to connect C_1 metabolism to NDDs. In animals, GTPCH catalyzes the first and limiting step in the tetrahydrobiopterin (BH_4) biosynthesis, and the latter serves as a cofactor for the production of the monoamine neurotransmitters [17]. Therefore, we set out to validate our novel findings from Htt_{ex1}Q63 transgenic plants in the well-established R6/2 HD mice. We discovered that $mHtt_{ex1}$ truly suppressed the levels of GTPCH as well as dihydrofolate reductase (DHFR), the key enzyme of folate utilization and alternate BH_4 biosynthesis [15, 17], and disturbed C_1 and BH_4 metabolism in 4-week-old R6/2 mice.

Results

Generation of *mHtt*$_{ex1}$ transgenic plants

Htt_{ex1} with expanded "CAG" repeats that have been confirmed to be toxic and cause protein aggregation is commonly used to create HD models [18, 19]. We, therefore, expressed human Htt_{ex1} (derived from wild-type *Htt*) with normal 21Q or abnormal 42Q or 63Q repeats, and a bacterial *uidA* gene encoding *β*-glucuronidase (GUS) (as a vector control) (Fig. 1A) in tobacco plants to produce transgenic plants named Htt_{ex1}Q21, Htt_{ex1}Q42, Htt_{ex1}Q63, and GUS, respectively. PolyQ63 dramatically affected the number of shoots per explant and leaf color, and hampered plant growth and development, but did not affect the tissue culture response nor the sizes of produced pods and seeds (Figs. S1 and S2). PolyQ42 had less negative effects, while polyQ21 displayed no negative effects compared to GUS. Transgenes were confirmed to be stably integrated into the tobacco genome by PCR and properly transcribed by RT-PCR analysis (Figs. 1B, C; S3). Immunoblotting analysis of two PCR-confirmed transgenic lines from each construct showed immunoreactive bands with sizes of ~ 20, ~ 26 and ~ 32 kD (Fig. 1D), twice their predicted sizes as also observed in a mouse HD model expressing N-terminal mHtt [20]. The authors [20] suggested that the Htt peptides with polyQ easily form di- and trimers. The obtained results indicate that these stable transgenic plants accumulated Htt peptides, each with the expected polyQ length, and that the toxic effects of polyQ tracts on plant growth are length-dependent.

PolyQ63 and polyQ42 cause protein aggregation

The presence of neuronal aggregates/inclusion bodies is a pathological hallmark in HD patients and models [19, 21,

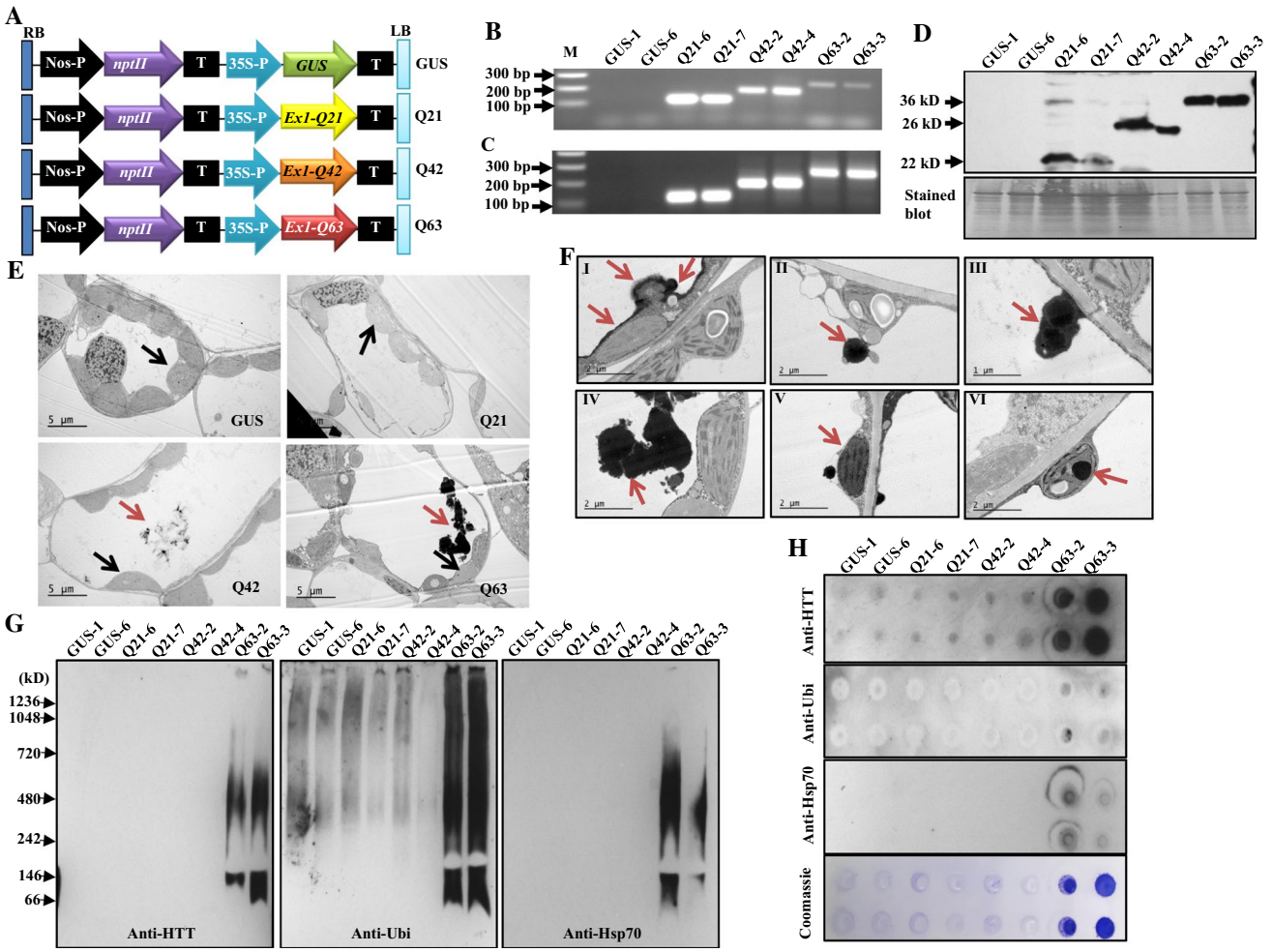

Fig. 1 Genetic cassettes and transgenic plant characterization. **A** Schematic representation of four genetic cassettes used to transform tobacco plants. **B-D** Representative results of two transgenic lines per genetic cassette analyzed by genomic PCR (B), RT-PCR (C), and immunoblotting with anti-Htt antibody (ab109115, Abcam) (**D**). M: DNA marker. The bottom panel of immunoblot (D) stained with Amido Black 10B to show protein loading. **E** Microstructures of transgenic leaf cells under electron microscope. Red arrows indicate protein aggregates while black arrows indicate chloroplasts. **F** Observation of different stages of aggregate formation in young leaves of Htt_{ex1}Q63 plants under TEM: initiated around chloroplasts and along the tonoplast (I), formed aggregates (II, III) released into the vacuoles (IV). They are also observed in cytoplasm (V) and inside of chloroplasts (VI). **G** Immunoblotting analysis of protein aggregates in young leave from two lines per genetic cassette by BN-PAGE. **H** Filter retardation assay of protein aggregates trapped on 0.2 µm membranes. One membrane was stained with coomassie R-250 (Coomassie) showing the presence of protein aggregates. Anti-HTT: anti-Huntingtin; Anti-Ubi: anti-Ubiquitin; and Anti-Hsp70: anti-Hsp70-biotin. Q21: Htt_{ex1}Q21; Q42: Htt_{ex1}Q42; and Q63: Htt_{ex1}Q63

22]. To determine whether overexpressing $mHtt_{ex1}$ could also cause protein aggregation, transgenic leaf cells were first used to observe aggregates. Aggregates were frequently observed in Htt_{ex1}Q63 young leaf cells while only small aggregates were occasionally found in a few Htt_{ex1}Q42 cells; whereas no aggregates were detected in either Htt_{ex1}Q21 or GUS cells (Fig. 1E). In Htt_{ex1}Q63, the aggregates were often localized in vacuoles, and appeared to initiate around chloroplasts and along the tonoplasts with a progressive increase in size and then release into vacuoles (Fig. 1F). They were also observed in the cytoplasm and inside of the chloroplasts (Fig. 1F). We also noticed that Htt_{ex1}Q63 had much smaller chloroplasts with roughly half the size of those observed in the GUS control (Fig. 1E).

Since $mHtt_{ex1}$, ubiquitin and Hsp70 were reported to be present inside polyQ-aggregates in mammalian cell and animal models of HD [22, 23], we investigated whether they are also present inside of the plant polyQ-aggregates by employing Blue Native-PAGE (BN-PAGE) immunoblotting and filter retardation assays. Both assays showed that $mHtt_{ex1}$, ubiquitin and Hsp70 were present in Htt_{ex1}Q63 lines (Fig. 1G, H), which are consistent with the observations made in mammalian cell and animal models [22, 23]. The observed length-dependent polyQ-aggregates and detected

mHtt$_{ex1}$, ubiquitin and Hsp70 inside aggregates indicate that the plant-based protein aggregation model recapitulates a major pathogenic process of HD reported in animal models [18, 19] and could be useful for dissecting the underlying mechanisms of mHtt-induced toxicity.

PolyQ63 affects root and root hair growth

Root hairs and neurons have been reported to share similar morphological and biochemical features [7, 8], and both the axon extension and root hair tip growth processes are tightly associated with tubular endoplasmic reticulum (ER) remodeling in the direction of cell elongation [8, 24–26]. During the subculture and propagation of transgenic plants, we paid special attention to root growth. We did observe slow growth of induced adventitious roots from Htt$_{ex1}$Q63 shoots with no root hairs in the maintenance medium (Fig. 2A, B). These phenomena prompted us to systematically investigate the effects of polyQ repeat length on adventitious root emergence and subsequent growth. We found that the percentages of shoots with emerging roots among the four types of transgenic lines were not different (Fig. 2C). However, emerging roots from Htt$_{ex1}$Q63 were shorter (~0.5 cm) and devoid of root hairs on day 11 of the subculture, whereas those from Htt$_{ex1}$Q42 had the same length (~3 cm) as Htt$_{ex1}$Q21 and GUS (Fig. 2D) but lesser root hair density (Fig. 2B). When the root hair emerging site from the root tip was measured, 43 out of 50 Htt$_{ex1}$Q63 roots had no root hairs while all Htt$_{ex1}$Q42, Htt$_{ex1}$Q21, and GUS roots had root hairs with distances of 2.2–2.6 cm (Fig. 2E). When root tips were observed in detail, most of the Htt$_{ex1}$Q63 root tips were found to be loosely organized while Htt$_{ex1}$Q42 and Htt$_{ex1}$Q21 root tips were intact, as in GUS (Fig. 2B). As observed in leaf cells, Htt$_{ex1}$Q63 root cells in the root apical meristem (RAM) area often contained aggregates while Htt$_{ex1}$Q42, Htt$_{ex1}$Q21, and GUS had only a few or no aggregates (Fig. 2F). These results confirm that mHtt also induces aggregation in RAM cells and affects root growth and root hair outgrowth.

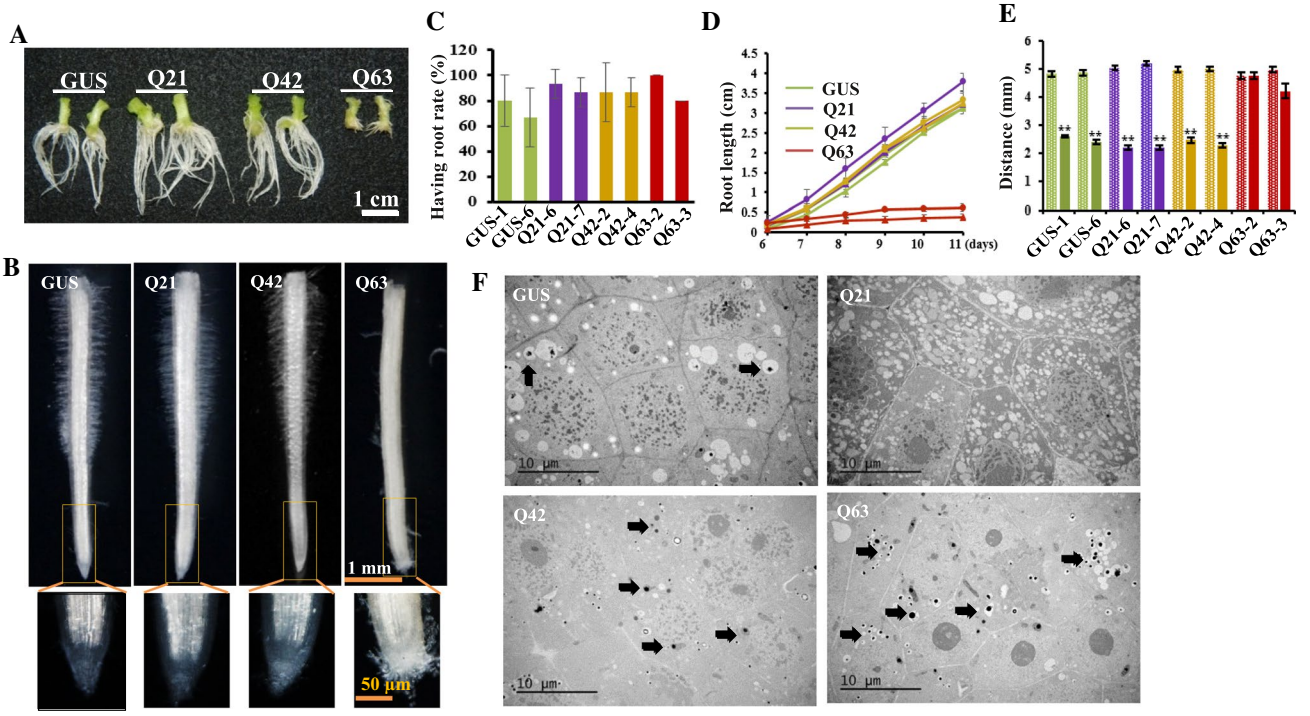

Fig. 2 Morphology and microstructures of induced adventitious roots. **A** Root morphology. **B** Root hair distribution in the ~5 mm root tip region and enlarged root tip structure. **C**, **D** Root emerging frequencies and root growth rates in subcultured shoots. Five shoots per line with two lines per genetic cassette were subcultured. The root emerging frequency was recorded at day 6 of subculture (**C**). The length of the longest root per plant was measured daily from day 6 till day 11 (**D**). The experiment was repeated three times. Both data plotted are the average of three independent experiments ± SD. **E** Root hair distribution. The full length of the longest induced root within 4–6 mm from each subcultured shoot (dotted bar) and the distance between the root tip and root hair emerging site (solid bar) were measured. Data plotted are the average of all observed roots ± SD (GUS: $n=29$ and 28; Htt$_{ex1}$Q21s: $n=25$ and 25; Htt$_{ex1}$Q42: $n=26$ and 28; Htt$_{ex1}$Q63: $n=21$ and 29). $^{**}p<0.01$ level. **F** Root cells at the root apical meristem (RAM) area from four transgenic lines observed under TEM. Arrow indicates protein aggregates. Q21: Htt$_{ex1}$Q21; Q42: Htt$_{ex1}$Q42; and Q63: Htt$_{ex1}$Q63

PolyQ63 remodels the proteome of roots

The significant differences in morphology and protein aggregation observed between $Htt_{ex1}Q63$ and $Htt_{ex1}Q21$ roots gave us an ideal pair of specimens for investigating toxic assault of polyQ-induced protein aggregation on cellular pathways. To gain insight into polyQ63-induced changes, a quantitative proteomic analysis was performed on $Htt_{ex1}Q63$ and $Htt_{ex1}Q21$ young roots (~0.5 cm). The proteomic results (Text S1; Fig. S4; Tables S1–S3) are summarized in Fig. 3A. 2D hierarchical clustering analysis of 5073 proteins quantified by ≥2 peptides (Table S4) indicates that extensive proteome remodeling occurred in $Htt_{ex1}Q63$ roots (Fig. 3B). Using the cutoff of abundance change ≥1.5-fold and an FDR-corrected $p < 0.05$, 1693 proteins were identified as DAPs with 854 abundance-increased and 839 abundance-decreased (Table S5). Gene Ontology (GO) analysis showed that polyQ63 mainly suppressed proteins involved in translation, folding, transport and localization, especially from the vesicle-mediated ER to the Golgi (Text S1; Fig. S5; Table S6). It also induced a large group of proteins associated with oxidative stress (Fig. S6; Table S7). Based on molecular function, polyQ63 primarily perturbed GTPases, RNA binding proteins and enzymes involved in

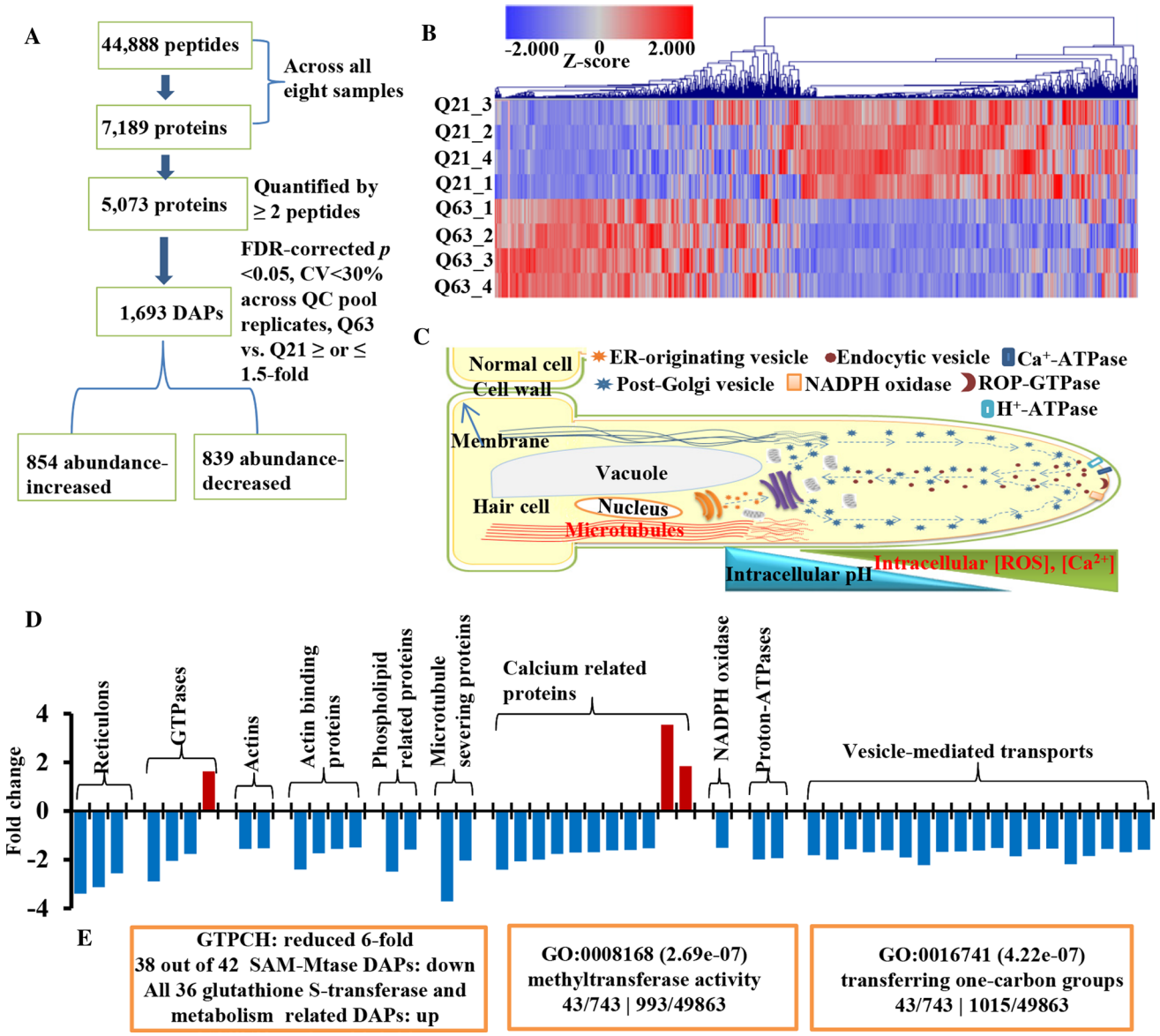

Fig. 3 Proteome of induced adventitious roots. **A** Proteomic comparison between $Htt_{ex1}Q63$ (Q63) and $Htt_{ex1}Q21$ (Q21) roots ($n=4$). **B** 2D hierarchical clustering analysis of the expression levels of 5073 proteins quantified by ≥2 peptides. **C** A schematic representation of a root hair cell showing essential cellular components for its elongation adopted from Balcerowicz et al. [31]. **D** Obtained DAPs involved in root hair elongation. **E** Affected major proteins and pathways (orange boxes) related to C_1 metabolism

C_1 group transfer (Fig. S5). In addition, 43 out of 49 mitochondria-related DAPs (Tables S8 and S9) were found to be abundance-increased. We, therefore, measured ATP levels in all four transgenic lines and detected significantly higher ATP levels in $Htt_{ex1}Q63$ than the other three lines (Fig. S7). A large group of identified abundance-increased mitochondria-related DAPs along with higher ATP levels observed in $Htt_{ex1}Q63$ indicates that cellular response to stress induced by polyQ63 is similar to what was observed in young HD mice with elevated levels of glycolysis and ATP [27], but different from those in old HD mice with dysfunctional mitochondria and low ATP [19, 28]. Our results revealed that polyQ63 extensively altered the root proteome and affected multiple cellular pathways as observed in other HD models [23, 29].

PolyQ63 affects key proteins involved in the root hair tip growth

Root hair tip growth resembles neuronal axon extension. There is continuous exocytosis of plasma membrane vesicles toward the tip, involving reconfiguration of the actin cytoskeleton and activation of actin-binding proteins and their upstream signals, such as calcium, phospholipids, and small GTPases (Fig. 3C) [30, 31]. In animals, GTPases interact with tubule-shaping proteins, reticulons and DP1/Yop1p, to form the tubular ER network for neurite elongation [24]. Our proteomics data showed that 47 out of 50 identified tubular ER network-related DAPs, including three reticulon-like proteins and three GTPases, were abundance-decreased (Fig. 3D; Table S10), supporting impaired root growth and root hair tip growth observed in $Htt_{ex1}Q63$ (Fig. 2A, B). However, root hair initiation was unaffected (Text S2), as evidenced by a 1.5-fold decrease in GLABRA2 (GL2) (Fig. S8B), a key inhibitory transcription factor controlling the differentiation of an epidermal cell into a root hair cell [30, 31]. This is also supported by induced adventitious roots from $Htt_{ex1}Q63$ shoots with root hairs when the shoots were inoculated on the surface of the maintenance medium (Fig. S8C).

A root tip can be divided into meristematic, transition and elongation regions based on their specialized functions and characteristic cellular activities (Fig. S9A) [31]. Our proteomic data provide supporting evidence for the observed results of stunted root growth and deformed root apex (Fig. 2A, B). We identified a large group of abundance-decreased DAPs that function in cell division, expansion and elongation (Fig. S9B) and ribosome biogenesis along with a group of ribosome assembly factors, glutathione-*S*-transferases (GSTs), DNA-directed RNA polymerases, serine/threonine-protein kinases, and phosphatases (Fig. S9C; Tables S11–14). A decrease in the abundances of these proteins may be responsible for defective root growth and root cap integrity, as discussed in Supplementary Text S3.

PolyQ63 also affects proteins whose mammalian homologs play critical roles in NDDs

A group of DAPs affected by polyQ63 whose mammalian homologs are well-known players in NDDs were identified (Table 1). GTPCH encoded by *GCH-1* gene was the most decreased enzyme (sixfold decrease) along with another member (UnitProt: W8TFR1, 2.5-fold decrease). In mammals, it plays an important role in the central nervous system by regulating the biosynthesis of BH_4, which acts as a cofactor for the production of several monoamine neurotransmitters [17]. GTPCH has not been reported to be directly involved in HD before. In humans, the deficiency of GTPCH was found to reduce dopamine synthesis and thought to contribute to an increased risk of developing Parkinson's disease [32]. The next was a huntingtin-interacting protein K (HYPK)-like (2.5-fold decrease) whose mammalian homolog is an HD hallmark protein preventing mHtt-induced aggregation and apoptosis [33]. The third was RHD3, a GTP-binding protein essential for root hair growth [34], which decreased by 1.8-fold. RHD3 is a homolog of human atlastin-1 [24–26] whose mutation causes hereditary spastic paraplegia [24]. Moreover, a K Homology (KH) domain-containing protein whose human homolog is involved in schizophrenia [35] was also reduced by 3.2-fold. In addition, 10 glutamate/GABA cycle-related enzymes [36] were found to be increased (Table 1), suggesting that polyQ63 also alters the glutamate/GABA-glutamine cycle in transgenic plants.

PolyQ63 impairs C_1 metabolic pathway enzymes

Importantly, our proteomic results also suggested alterations in C_1 metabolic pathways in the $Htt_{ex1}Q63$ transgenic roots (Fig. 3E), which comprises of the folate cycle, the methionine cycle, and the transsulfuration pathway [11, 12, 15], with the following evidences. First, GTPCH, a rate-limiting enzyme for plant folate biosynthesis (Fig. 4A) [37] decreased sixfold (Table 1), which could dramatically affect folate levels and impair C_1 metabolism. Next, $Htt_{ex1}Q63$ expression decreased the abundances of 38 out of 42 *S*-adenosyl methionine-dependent methyltransferases (SAM-MTases) (Table S15) and increased the abundances of all 36 GSTs and proteins involved in the regulation of glutathione redox status (Table S12). SAM-MTases play critical roles in the transfer of methyl groups to various biomolecules, while GSTs regulate redox status [11, 12]. These results imply that polyQ63 disturbs the methionine cycle and transsulfuration pathways of C_1 metabolism. GO analysis of abundance-decreased DAPs also showed significant

Table 1 DAPs homologous to mammalian proteins associated with NDDs and involved in glutamate, GABA and glutamine metabolism

UniProtKB	Protein description	Log2 fold-change	*p* value[a]
A0A1S3WYB9	GTP cyclohydrolase 1	− 2.64	0.002
W8TFR1	GTP cyclohydrolase II	− 1.32	2.5E−05
A0A1S4DLE6	Huntingtin-interacting protein K-like	− 1.34	0.001
A0A1S4DQ39	Protein ROOT HAIR DEFECTIVE 3 homolog	− 0.82	4.9E−05
A0A1S4CML3	KH domain-containing protein At1g09660/At1g09670-like	− 1.70	6.3E−05
Glutamate, GABA and glutamine metabolism			
A0A1S4DRP0_TOBAC	Gamma aminobutyrate transaminase 3, chloroplastic-like isoform X1	1.79	1.3E−05
A0A1S3ZU19_TOBAC	Glutamate dehydrogenase A-like	1.08	5.7E−05
A0A1S4AZM4_TOBAC	Glutamate–glyoxylate aminotransferase 2-like	1.07	5.0E−05
A0A1S4A4G8_TOBAC	Ferredoxin-dependent glutamate synthase 1, chloroplastic/mitochondrial-like	0.89	4.5E−04
A0A1S4AWH0_TOBAC	Glutamine synthetase	0.84	5.1E−04
Q7M242_TOBAC	Glutamate synthase (Ferredoxin) (Clone C(35)) (Fragment)	0.83	6.6E−04
A0A1S4AUA9_TOBAC	Bifunctional aspartate aminotransferase and glutamate/aspartate-prephenate aminotransferase-like	0.83	1.0E−03
A0A1S3Z1F3_TOBAC	Ferredoxin-dependent glutamate synthase, chloroplastic-like	0.82	5.8E−04
A0A1S4B8W9_TOBAC	Glutamate dehydrogenase	0.82	3.1E−04
A0A1S4AZA4_TOBAC	Gamma aminobutyrate transaminase 1, mitochondrial isoform X1	0.80	7.6E−04

[a] *t* test with FDR correction

enrichment of methyltransferase activity and C_1 transfer pathways (Figs. 3E; S5). In conclusion, our results showed that polyQ63 impairs GTPCH and many other proteins associated with C_1 metabolism in the young roots. These findings are novel and valuable for understanding early mHtt-induced pathophysiological changes since GTPCH is a rate-limiting enzyme for de novo folate biosynthesis in plants while folate-mediated C_1 metabolism is essential for cell survival and proliferation in both animals and plants by providing C_1 units to various biosynthetic and methylation processes [11–16].

mHtt impairs GTPCH and DHFR in young HD mice

We then set out to validate whether the novel findings of mHtt-impaired GTPCH expression and C_1 metabolic pathways in $Htt_{ex1}Q63$ plants are true in R6/2 mice, a well-established HD animal model [38]. GTPCH catalyzes the same reaction involving the conversion of GTP to dihydroneopterin triphosphate (DHPTP) in both mammals and plants [37, 39]. However, the DHPTP produced in plants is converted into dihydrofolate to enter the folate cycle, while it is converted into BH_4 in mammals to serve as a cofactor for several hydroxylases; these hydroxylation reactions produce monoamine neurotransmitters with concomitant oxidation of BH_4 to dihydrobiopterin (BH_2) (Fig. 4A). BH_2 is then rapidly reduced back to BH_4 by quinoid dihydropteridine reductase (QPDR) or DHFR when QPDR is limiting [40]. The main function of DHFR in animals is to generate a metabolically active form of tetrahydrofolate (THF) from diet-derived folic acid to enter the folate cycle [41] while its reductive function also interconnects folate metabolism to biopterin metabolism [40]. Hence, we analyzed both GTPCH and DHFR, as well as nine other C_1 and BH_4 metabolism-related enzymes (Fig. 4A), in the brains of 4-week-old male R6/2 mice.

In HD, the most affected organ is the brain, especially the striatum and the cortex [4, 21]. Four-week-old R6/2 mice (Fig. S10A) showed no differences in body weight, brain weight or striatum size compared to the noncarrier (NCAR) control animals (Fig. S10B–S10E), but did display mHtt-containing protein aggregates in both the striatal and cortical regions (Fig. 4B). Notably, western blotting results showed that R6/2 brain tissues had significantly decreased expression levels of GTPCH and DHFR, as well as of methionine synthase (MS) and methionine adenosyltransferase (MAT1/2A), but no change in the expression levels of QPDR, methylene-tetrahydrofolate reductase (MTHFR), or *S*-adenosylhomocysteine hydrolase (AHCY) (Fig. 4C, D). In addition, the levels of all three BH_4-dependent enzymes tryptophan hydroxylase (TPH2), tyrosine hydroxylase (TH) and neuronal nitric oxide synthase (nNOS) for the synthesis of serotonin, dopamine and nitric oxide were all significantly decreased, but not of BH_4-independent choline acetyltransferase (ChAT) (Fig. 4C, D). These results not only confirmed that the $mHtt_{ex1}$-impaired GTPCH expression discovered in mHtt transgenic plant system is also true in young R6/2 mice, but also revealed that the $mHtt_{ex1}$ impaired the expression of DHFR at this juvenile stage.

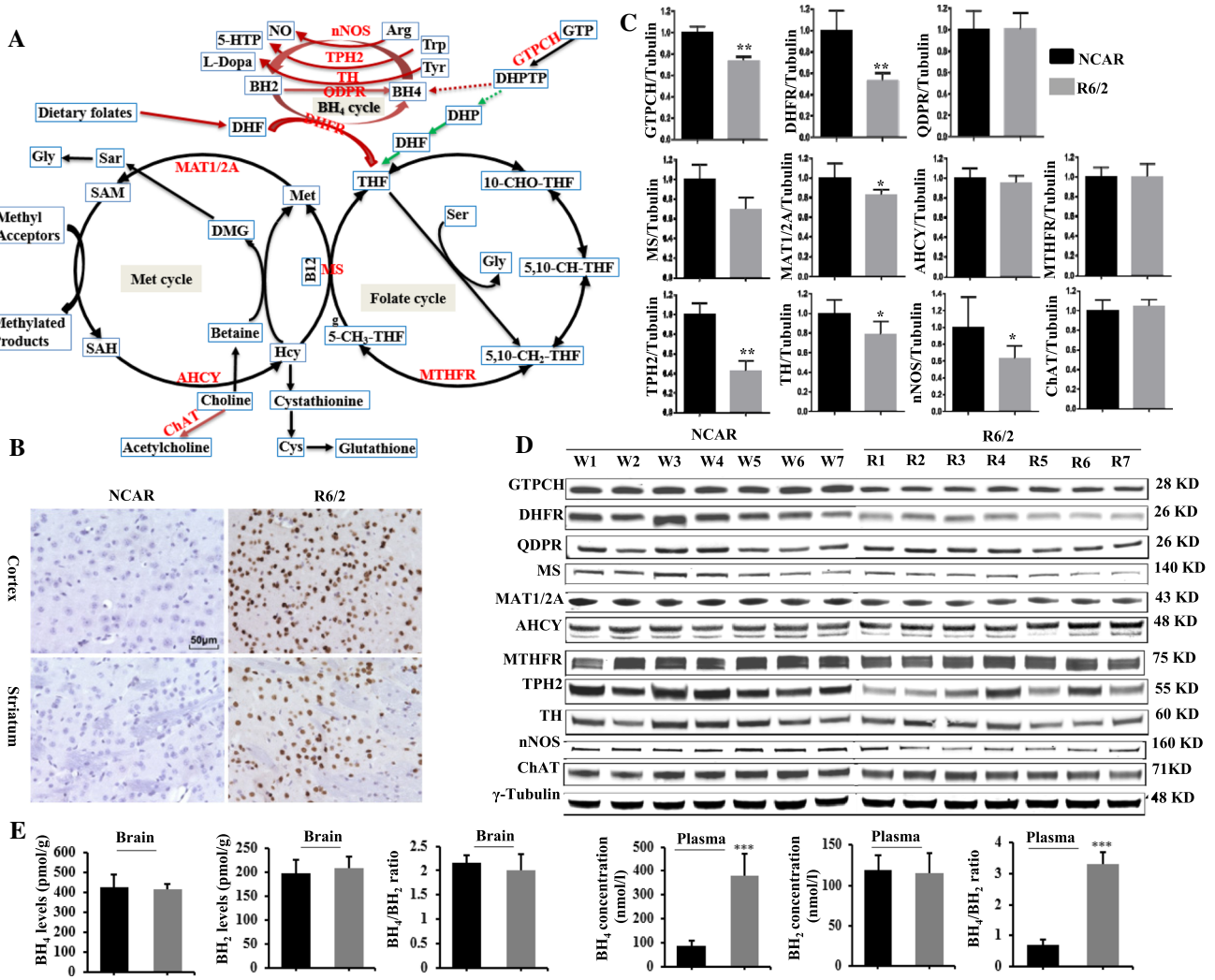

Fig. 4 C_1 metabolic pathway and characterization of R6/2 mice. **A** Folate, Met and BH_4 cycles in plants and animals and their associated metabolism. Red lines stand for mammal specific, green lines stand for plant specific while black lines stand for both. All enzymes with protein levels examined by immunoblotting are marked in red. **B** mHtt protein aggregates in cortex and striatum regions were detected with anti-Htt antibody (mEM48) in 4-week-old male R6/2 and NCAR mice. **C**, **D** Quantification analysis of immunoblotting results of GTPCH, DHFR, QDPR, MS, MAT1/2A, AHCY, MTHFR, TPH2, TH, nNOS and ChAT ($n=7$). The band intensity of each protein from western blotting **D** was normalized with γ-tubulin on the same blot. The ratio was further calculated against NCAR whose relative expression level was set as 1. All data plotted are the average ($n=7$) ± SD. Only one representative western blotting of γ-tubulin is shown. Original blots of above proteins before cropping are presented in Fig. S11. **E** Contents of BH_4 and BH_2, and their ratio in brain tissues and plasma ($n=4$, average ± SD). $*p<0.05$; $**p<0.01$. $***p<0.001$. Abbreviations used for enzymes: *AHCY* *S*-adenosylhomocysteine hydrolase, *ChAT* choline acetyltransferase, *DHFR* dihydrofolate reductase, *GTPCH* GTP cyclohydrolase I, *MAT1/2A* methionine adenosyltransferase, *MS* methionine synthase, *MTHFR* methylene-tetrahydrofolate reductase, *nNOS* neuronal nitric oxide synthase, *QDPR* quinoid dihydropteridine reductase, *TH* tyrosine hydroxylase (Tyr), *TPH2* tryptophan hydroxylase

mHtt affects GTPCH and DHFR expression in striatum and cortex differently

Striatum and cortex were found to be affected by mHtt differently [4, 21, 42]; and transcriptional levels of *GCH1* and *DHFR* were observed to be different in the basal ganglia and cortex of the human brain [17]. Since GTPCH and DHFR are critical enzymes for BH_4 biosynthesis and C_1 metabolism, they were further analyzed in the striatum and cortex separately. Western blotting results showed that the expression of DHFR was significantly decreased in both regions while, surprisingly, the GTPCH level was decreased in the cortex, but increased in the striatum compared to those of NCAR control (Fig. 5A). The increase of GTPCH in the striatum and decrease in the cortex while the decrease of DHFR in both regions were further confirmed by immunohistochemistry assay (Fig. 5C–F). These results indicated that GTPCH and DHFR are affected

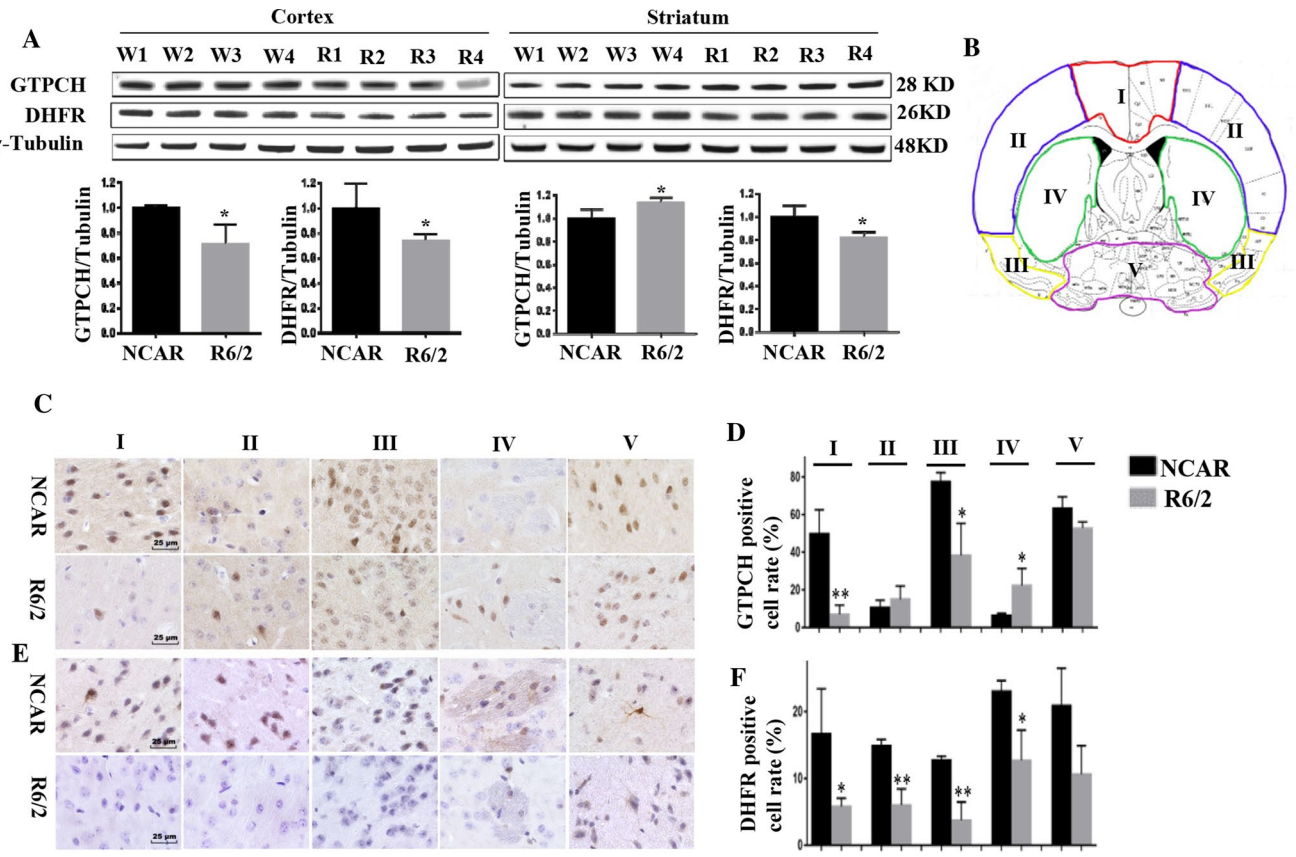

Fig. 5 Western blotting and immunohistochemistry assay of cortex and striatum regions to quantify GTPCH and DHFR expressions. **A** Immunoblotting of GTPCH and DHFR in the cerebral cortex and striatum tissues of R6/2 and NCAR mice using γ-tubulin as internal control ($n=4$). Protein bands were quantified as described in Fig. 4. Original blots before cropping are presented in Fig. S12. **B** Diagram of mouse brain section divided into five regions: three regions of cortex (I-III); striatum (IV); hypothalamus and pallidum (V). **C**, **D** GPTCH and **E**, **F** DHFR positive cells and their ratios were quantified in five regions (I–V). $*p<0.05$; $**p<0.01$

differently by $mHtt_{ex1}$ in the striatum and cortex at an early stage.

mHtt alters C_1 and BH_4 metabolism in young R6/2 mice

We further measured BH_4, BH_2 and free amino acid levels in both plasma and brain tissues of 4-week-old R6/2 mice to investigate any changes that may be related to impaired expression of GTPCH and DHFR. The results showed that BH_4 was significantly increased by 4.5-fold in plasma but no change in brain tissues yet, while BH_2 remained unchanged in both plasma and brain tissues (Fig. 4E). Although there was no reduction in BH_4 in brain tissues, the dramatic increase in plasma could be the body's response to its declining cerebral levels of BH_4 since it can cross the blood–brain barrier [43]. The other reasons for no observed change in brain BH_4 levels could be that residual enzymatic activity of GTPCH is still high enough for BH_4 biosynthesis or its biosynthesis might be compensated by the other alternate de novo or/and salvage pathways [17].

We also measured the levels of free amino acids in both plasma and brain tissues with particular emphasis on Ser and Gly, as well as aromatic amino acids (Phe, Tyr, Trp). The former two provide C_1 units to various biomolecules while the latter three serve as substrates for monoamine neurotransmitters. We detected 29 free amino acids in plasma and 26 in brain tissues (Table 2). We divided these amino acids into four groups based on their major involvement in the central nervous system: group I, sources of C_1 units; group II, related to neurotransmitters; group III, branched-chain amino acids; and group IV, others. Among the five members in group I, Gly and Ser are the major sources of C_1 units [44, 45]. Gly was increased significantly by 26.5% ($p=0.014$) in the brain tissues, while Ser showed a marginally significant increase of 17.9% ($p=0.113$) in plasma. In the folate cycle, Gly and Ser fuel mitochondrial enzymes through purine production [12, 15]. These results indicate that the C_1 source in R6/2 mice was disrupted by $mHtt_{ex1}$ at this early stage,

Table 2 The contents of amino acids in R6/2 and NCAR mouse brain tissues and plasma

Group[a]	Amino acids	Brain tissues			Plasma		
		NCAR (μmol/L)	R6/2 (μmol/L)	Changes[b] (%) (*p* value)	NCAR (μmol/L)	R6/2 (μmol/L)	Changes[b] (%) (*p* value)
I	Ser	882.8 ± 104.6	894.9 ± 19.9	1.4 (0.827)	126.7 ± 19.0	149.3 ± 15.3	17.9 (0.113)
	Gly	947.8 ± 65.0	1199.1 ± 131.7	**26.5 (0.014)**	432.1 ± 44.0	472.7 ± 53.3	9.4 (0.284)
	His	87.1 ± 15.2	86.7 ± 12.7	− 0.5 (0.967)	59.2 ± 8.8	70.3 ± 12.0	18.8 (0.187)
	Thr	362.4 ± 13.5	390.4 ± 27.8	7.7 (0.120)	167.3 ± 29.8	176.8 ± 13.5	5.7 (0.583)
	Met	77.0 ± 4.7	70.8 ± 12.3	− 8.1 (0.382)	59.1 ± 8.6	60.1 ± 3.7	1.6 (0.844)
II	PEA	2050.1 ± 41.7	2184.2 ± 88.4	**6.5 (0.034)**	11.6 ± 5.6	12.3 ± 8.0	5.7 (0.896)
	EA	75.6 ± 18.9	71.5 ± 11.1	− 5.4 (0.722)	12.6 ± 2.0	11.3 ± 2.6	− 10.1 (0.469)
	Phe	62.8 ± 15.0	84.4 ± 14.4	34.4 (0.083)	54.8 ± 8.6	58.5 ± 4.3	6.8 (0.471)
	Tyr	89.8 ± 15.6	91.4 ± 5.7	1.7 (0.859)	64.8 ± 5.3	67.4 ± 5.1	4.0 (0.505)
	Trp	53.4 ± 16.9	54.9 ± 2.8	2.8 (0.867)	61.2 ± 6.0	58.7 ± 5.9	− 4.0 (0.580)
	Arg	157.5 ± 35.7	153.1 ± 18.4	− 2.8 (0.832)	76.0 ± 24.5	105.0 ± 27.7	38.2 (0.168)
	Gln	5148.3 ± 308.6	5792.2 ± 317.1	**12.5 (0.027)**	486.5 ± 68.9	443.1 ± 44.6	− 8.9 (0.331)
	AADA	107.4 ± 10.7	161.7 ± 41.2	**50.5 (0.044)**	3.1 ± 0.8	8.8 ± 8.4	179.7 (0.229)
	Glu	10,685.5 ± 464.4	11,235.4 ± 117.8	5.1 (0.062)	49.7 ± 17.7	47.9 ± 23.5	− 3.5 (0.910)
	Asp	2640.4 ± 251.9	2604.2 ± 131.4	− 1.4 (0.808)	10.6 ± 4.0	13.1 ± 7.9	23.1 (0.598)
	GABA	3478.8 ± 343.2	3700.0 ± 228.4	6.4 (0.325)			
	Ala	1163.8 ± 131.1	1094.6 ± 57.1	− 5.9 (0.371)	658.0 ± 161.0	780.9 ± 149.9	18.7 (0.306)
	β-Ala	66.3 ± 3.5	68.0 ± 2.3	2.6 (0.435)	5.7 ± 0.9	5.8 ± 0.6	1.2 (0.902)
	Carn	117.7 ± 48.4	110.4 ± 32.6	− 6.2 (0.810)			
	Asn	97.3 ± 10.4	104.7 ± 7.5	7.6 (0.291)	39.9 ± 8.6	45.7 ± 5.3	14.4 (0.298)
	Pro	126.7 ± 15.0	143.8 ± 7.7	13.5 (0.088)	104.6 ± 18.9	125.2 ± 14.8	19.7 (0.137)
	Lys	322.0 ± 16.6	304.1 ± 17.3	− 5.6 (0.184)	305.0 ± 45.8	365.8 ± 6.6	**19.9 (0.039)**
III	Val	153.0 ± 18.4	175.8 ± 14.7	14.8 (0.102)	221.1 ± 25.4	267.5 ± 28.9	21.0 (0.053)
	Ile	61.9 ± 13.3	74.6 ± 11.3	20.5 (0.196)	93.1 ± 10.8	120.5 ± 18.8	**29.3 (0.045)**
	Leu	109.4 ± 22.3	144.3 ± 23.5	31.8 (0.075)	118.3 ± 10.2	143.7 ± 22.4	21.5 (0.084)
IV	Tau	12,223.6 ± 633.3	13,056.9 ± 853.3	6.8 (0.163)	564.9 ± 166.5	448.9 ± 158.5	− 20.5 (0.352)
	AABA				4.6 ± 1.0	6.0 ± 0.7	30.1 (0.058)
	HyPro				48.0 ± 10.2	58.9 ± 9.5	22.7 (0.169)
	Cit				65.1 ± 10.0	58.4 ± 7.0	− 10.3 (0.313)
	Sar				110.4 ± 22.8	117.2 ± 3.8	6.1 (0.581)
	Orn				97.9 ± 43.9	85.1 ± 14.8	− 13.1 (0.599)

[a]I. Sources of C_1 units; II: Related to neurotransmitters; III. Branched-chain amino acids; and IV. Others

[b]Amino acid level changes in R6/2 mice compared to NCAR mice. Any significant difference with $p < 0.05$ is shown in bold

which might potentially lead to mitochondrial dysfunction at the later stage.

Among group II amino acids involved in neurotransmission, PEA, Gln and AADA were found to be significantly higher ($p < 0.05$), while Phe, Glu and Pro were less significantly higher ($p < 0.1$) in brain tissues of R6/2 mice than NCAR control. In mammals, Phe is an essential amino acid and also serves as an important precursor of Tyr requiring BH_4 as a cofactor for the synthesis of monoamine neurotransmitters [32, 39, 46], while PEA regulates monoamine neurotransmission in neurons [47]. However, there was no change in the contents of the three other monoamine neurotransmitter precursors Tyr, Trp and Arg in brain tissues yet. Concerning elevated Gln, Glu and Pro, they play important roles in the Gln/Glu (GABA) cycle [48, 49]. In regard to elevated AADA, it is a 6-carbon homologue of Glu and generated from the catabolism of Lys [50, 51]. Lys was significantly increased (~ 20%) in R6/2 plasma. It is not clear whether there is any relation between high plasma level of Lys and elevated AADA content in brain tissues, but the elevation of the latter in the brain tissues could exert its toxicity via enhanced release or transport of excitatory Glu [50, 51]. Undeniably, the increase of these amino acids along with the decreased levels of three BH_4-dependent neurotransmitter synthases (Fig. 4C, D) implies that neurotransmitter biosynthesis or metabolism in 4-week-old R6/2 mice was perturbed by $mHtt_{ex1}$.

Group III comprises of three proteinogenic branched-chain amino acids (Ile, Leu and Val), which are essential to build muscle [52]. They were reported to be reduced in the plasma of the middle- to aged-HD patients and sheep and thus proposed to be potential biomarkers of HD because their reductions were correlated with weight loss and disease progression [52–54]. In the current study, they were all substantially increased in both brain tissues and plasma of young R6/2 mice. The increase in these amino acids in the early stage could be a stress response to counteract the toxic effects of mHtt and was consistent with no body weight loss in young R6/2 mice (Fig. S10B). The contradiction between our results and previous reports implies that mHtt-induced metabolic dysfunction in the early growth stage is different from that in the middle and late growth stages. Nevertheless, elevated levels of amino acids and their derived products have been reported as pathogenic factors for neurological disorders [55]. The observed changes in plasma BH_4 and the above amino acids indicate that $mHtt_{ex1}$ alters BH_4 and C_1 metabolisms in young R6/2 mice.

Discussion

Although plants have not been previously considered to be used to study NDDs, our studies demonstrate that the plant-based system with polyQ-induced protein aggregation is unique and valuable for studying expanded polyQ-mediated toxicity. In the current study, our approaches involved establishing stably transgenic tobacco plants carrying *mHtt-t*$_{ex1}$, observing polyQ length-dependent toxic effects, discovering mHtt-affected proteins and cellular pathways, and finally verifying novel findings from the plant-based system in young R6/2 mice. In transgenic plants, we observed that the toxic effects of expanded polyQ on protein aggregation and plant growth, especially root and root hair development, resemble those reported in animal HD models in a polyQ length-dependent manner [18, 19]. It is likely that all observed toxic effects are results from gain-of-function of mHtt as plants lack endogenous Htt. Importantly, using this plant-based system allowed not only the identification of many homologous proteins known to be affected by expanded polyQ in neuronal cells but also the discovery of hitherto unreported mHtt-mediated disturbance of GTPCH and its associated C_1 metabolism, which could be an early event in the pathogenesis of mHtt. These findings empower autotrophic plants with de novo synthesis of folate [11, 12] to be a good system for studying mHtt-impaired folate and C_1 metabolic pathways.

Because of the evolutionary distance between plants and mammals, it is essential to validate mHtt-impaired GTPCH expression and C_1 metabolism in an HD animal model to confirm the usefulness of the plant-based polyQ system. In animals, GTPCH controls the biosynthesis of BH_4 [39], an essential cofactor for amino acid hydroxylases to produce monoamine neurotransmitters [32, 39] while DHFR plays dual roles in the folate and BH_4 cycles (Fig. 4A) [40, 41]. Our validation studies confirmed that the expression levels of both GTPCH and DHFR were suppressed in total brain tissues (Fig. 4C). Unexpectedly, using plant and animal HD systems together led to the discovery of impaired expression of GTPCH and DHFR, which have not been directly linked to HD before. Only recent genome-wide association studies with genetic information from a large number of HD patients predicted that DHFR is possibly a modifier of disease progression [5, 56]. In addition, genetic defects in DHFR were found to cause insufficient cerebral BH_4 levels [40], while GTPCH-deficient mice exhibited BH_4-related metabolic disturbance and infancy-onset motor impairments [57]. These previous reports point to the importance of maintaining normal expression of GTPCH and DHFR in animals. The current study provides direct evidence that mHtt impairs these two key enzymes of C_1 and BH_4 metabolisms. The toxic effects of mHtt on GTPCH and DHFR are also supported by the observed interruption of C_1 and BH_4 metabolism in young R6/2 mice. Although there was no decrease in BH_4 levels in brain tissues, the dramatic increase in plasma BH_4 levels and the decrease in three BH_4-dependent aromatic amino acid hydroxylases imply declining cerebral levels of BH_4 at this young stage (Fig. 4E). In addition, we observed elevated levels of several amino acids serving as major sources of C_1 units or precursors for neurotransmitter synthesis (Table 2). Taken together, our study revealed that GTPCH- and DHFR-associated C_1 and BH_4 metabolism and neurotransmitter biosynthesis were disturbed by mHtt at a very early stage.

In the case of inherited polyQ diseases, polyQ-induced cellular damage by the time any disease symptoms appear might already be too advanced for the treatment to be successful. Thus, any strategy preventing the development of diseases or impeding the progression of diseases early will be a promising avenue for improving health and quality of life for mutant gene carriers. Our findings of early polyQ-affected GPTCH and DHFR, and their related cellular pathways are significant because disordered transcriptomes and altered epigenetics have been reported to be common HD-induced pathological changes [6, 58, 59]. Decreased the abundances of DHFR, 38 SAM-MTases and 16 nucleolar proteins together with changed the abundances of 10 histone related DAPs in Htt_{ex1}Q63 roots (Table S15) by mHtt provide a clue to understanding how mHtt affects C_1 metabolism and the flux of methyl groups, leading to potentially low methylation activity, and subsequently causing transcriptional dysregulation and epigenetic alteration. Previous studies suggest that the alteration of epigenetic components and the deregulation of transcriptional machinery resulted

from the impaired nucleolar activity and integrity are directly involved in HD pathogenesis and neuronal damage [60]. In plants and mammals, the folate metabolic pathway generates and provides methyl groups for methionine biosynthesis from homocysteine. More than 80% of synthesized methionine is further converted to SAM, which is a universal methyl donor for methylation reactions leading to the synthesis of many biomolecules and epigenetic regulation of gene expression via DNA and histone methylation [11, 12]. In addition, the observed opposite expression of GTPCH in the cortex and striatum in young R6/2 mice (Fig. 5) could be also notable. Under healthy conditions, the cortico-striatal system is tightly regulated by dopamine [42, 61]. mHtt-mediated opposite expression of GTPCH in the striatum and cortex may cause imbalance of the cortico-striatal system through dysregulation of dopamine and contribute to the selective vulnerability of striatal medium-spiny neurons to toxic polyQ repeats [42, 61]. Aberrant communication between striatum and cortex has been considered to play a critical role in striatal neuronal loss [4, 42]. It is not clear at this time how $mHtt_{ex1}$-mediated protein aggregation affects GTPCH expression in plants and animals. $Htt_{ex1}Q63$ transgenic plants created with dramatic changes in the abundance of GTPCH together with HD animal models could be used to further understand the relationship between the neurotoxicity and early polyQ-mediated alterations of C_1 and BH_4 metabolisms, epigenetics and transcriptomes, which may allow to identify therapeutic targets and develop preventive strategies for HD.

In addition, neuronal loss is a common pathological hallmark of HD and many other NDDs [1, 2]. Root hairs and neuronal cells share some strikingly similar characteristics, such as polarity, long extension outgrowth, high energy demand, and environmental sensing capacity [7, 8]. Observation of restricted root hair outgrowth in $Htt_{ex1}Q63$ roots and partially restricted in $Htt_{ex1}Q42$ roots means that root hairs might also respond to toxic polyQ repeats similar to neuronal cells. In particular, many affected components of tubular ER network that were identified in $Htt_{ex1}Q63$ roots (Fig. 3D; Table S10) are known to play crucial roles in neurite elongation. These results suggest that toxic polyQ repeat-induced neuronal loss and restricted root hair outgrowth may share some common mechanism(s). With the recent seminal discovery in adult neurogenesis that the adult brain is able to make new neurons throughout adulthood [62], our results that expanded polyQ repeat restricted root hair outgrowth (Fig. 2B, E), but did not affect hair initiation (Fig. S8B and S8C) may provide another piece of useful information for future polyQ-mediated NDD study. While many study the mechanisms of expanded polyQ-induced age-dependent progressive neurodegeneration, we should pay attention to the toxic effects of polyQ repeats on neuronal development and neurite outgrowth.

In summary, our study demonstrated for the first time, to the best of our knowledge, that expanded polyQ63-triggered protein aggregation in plant cells is akin to that in mammalian cells with many affected plant proteins homologous to mammalian ones, which play critical roles in NDDs. The obtained results from both plant and animal studies proved the concept that the plant-based protein aggregation system is useful for studying abnormal polyQ-mediated cellular toxicity in general and dysregulation of C_1 metabolism in particular. Given the importance of C_1 metabolism and the BH_4 cycle [13, 15, 39], the observed changes in GTPCH, DHFR, and certain C_1/BH_4 metabolism-related enzymes and metabolites in young HD mice could be significant contributing factors to HD onset and progression. Our findings from plant-based and R6/2 HD models open a new avenue to study the roles of GTPCH, DHFR, and C_1 and BH_4 metabolism in the initiation and progression of HD, and perhaps of other polyQ diseases.

Materials and methods

Plant materials and transgenic plant maintenance

Tobacco (cultivar "W38") plants were used to generate transgenic plants. Leaf explants from 4-week-old young plants prepared from seedlings were used for transformation. Methods of seed sterilization and leaf explant transformation were the same as described previously [63]. All PCR-confirmed transgenic plants were propagated and maintained on a maintenance medium (MS medium supplemented with 100 mg/L Timentin) under reduced light conditions of ~ 15 µmol/m^2/s photoperiod (16 h/day) at 23 °C because $Htt_{ex1}Q63$ plantlets showed stress symptoms with yellowish colored leaves and slow growth when grown under ~ 60 µmol/m^2/s light intensity. For each genetic cassette, seven independent transgenic lines were selected for propagating genetically identical plants from each line for downstream study. To achieve that, a shoot (~ 3 cm) was first cut and placed in MS medium for rooting. The remaining base part of the plant with several nodes was continually subcultured for 2 weeks to obtain additional new shoots. Propagated plants from each transgenic line were used for downstream studies. Transgenic plants grown in soil were also maintained under reduced light intensity conditions.

Construction of genetic cassettes

Three DNA sequences having 283, 346 and 409 bp encoding truncated Htt N-terminal fragments with 21Q, 42Q and 63Q repeats (GenBank Accession #: MK291497-MK291499), respectively, were synthesized (Life Technologies) by adding *Xba*I and *Sac*I restriction enzyme cutting sites at the 5′ and

3′ ends of each DNA sequence for sub-cloning. They were cloned into the plant expression vector pBI121 by replacing the bacterial *uidA* gene. Resultant three genetic cassettes were named as Htt_{ex1}Q21, Htt_{ex1}Q42 and Htt_{ex1}Q63, which were introduced into *Agrobacterium tumefaciens* strain LBA4404 using the freeze–thaw method [64].

Agrobacterium-mediated transformation

Among plants, the tobacco plant is well suited for this study because of its well-studied physiology and biochemistry, ease of genetic engineering with high transformation efficiency, and sufficient duplication of identical transgenic plants for various downstream studies [65, 66]. *Agrobacterium*-mediated leaf disc transformation [67] was employed for creating transgenic plants with the same protocols as described previously [63]. To study the transformation efficiencies of three genetic cassettes, Htt_{ex1}Q21, Htt_{ex1}Q42 and Htt_{ex1}Q63, approximately 20 leaf discs were used for each cassette. The original pBI121 plasmid DNA with *uidA* gene encoding β-glucuronidase (GUS, designated as "GUS") was used as a transformation control. For statistical analysis, 20 infected leaf discs were evenly cultured onto four selection plates, and each plate was calculated as one replicate. Infected leaf discs were transferred onto new media every 2 weeks. At the end of the second transfer, the numbers of induced calluses and shoots were recorded. The total transformed response was calculated as the number of responding explants (either with kanamycin-resistant calluses, shoots, or both) divided by the total inoculated explants. The transformation efficiency experiment was repeated three times. All leaf discs were maintained in a growth chamber under ~ 60 µmol/m^2/s light intensity at 25 °C.

Genomic DNA PCR analysis

To confirm the presence of integrated Htt_{ex1} with different "CAG" repeats and the kanamycin-resistance gene *nptII* in kanamycin-resistant plants, PCR amplifications were performed. To detect Htt_{ex1} with different "CAG" repeats, a pair of primers HDJamaF: 5′-ATGAAGGCCTTCGAGTCCCTC AAGTCC-3′ and HDJamaR2: 5′-CGGCGGCGGCGGTGG CGGCTGTT-3′ [68] was used. For detecting *nptII*, a pair of primers, NPT-II 5′: 5′-GTGGATCCCGCATGATTGAA-3′ and NPT-II 3′: 5′-TCGGATCCCTCAGAAGAACT-3′, was used. For each construct, seven independent transgenic lines were analyzed. Total genomic DNA was isolated from young leaves using a DNeasy® Plant min Kit (Qiagen). The DNA concentration was measured using an ND-1000 spectrophotometer (NanoDrop Technologies). For *nptII* detection, each 25 µL reaction mixture contained 100 ng DNA template, 2.5 µL of 10 × PCR buffer, 1.25 units of Taq DNA polymerase (Sigma-Aldrich), and final concentrations of 0.2 mM dNTPs, 300 nM of each primer and 2 mM $MgCl_2$. PCR cycles consisted of an initial denaturing step of 94 °C for 2 min, followed by 30 amplification cycles of denaturation at 94 °C for 1 min, annealing at 55 °C for 60 s and elongation at 72 °C for 30 s, and a final extended elongation at 72 °C for 10 min. To amplify Htt_{ex1} with different "CAG" repeats, each 30 µL reaction mixture contained 100 ng DNA template, 3 µL of 10 × homemade PCR buffer [69], 1.5 units of Taq DNA polymerase (Sigma-Aldrich), and final concentrations of 0.25 mM dNTPs, 300 nM of each primer and 2 mM $MgCl_2$. PCR cycling conditions consisted of an initial denaturing step of 96 °C for 3 min, followed by 35 amplification cycles of denaturation at 96 °C for 45 s, annealing at 64 °C for 45 s and elongation at 72 °C for 1 min, plus the final extended elongation at 72 °C for 10 min. PCR was performed on a TGradient Thermocycler (Biometra). Amplified DNA was resolved in a 1.0% agarose gel and visualized under UV light using UVP GelDoc-It™ Imaging Systems (Analytik Jena).

RT-PCR analysis

To detect Htt_{ex1} transcripts with different "CAG" repeats in transgenic plants, RT-PCR was used. Total RNA was isolated from young leaves using an RNeasy Plant Mini Kit (Qiagen). First strand cDNAs were made using a High-Capacity cDNA Reverse Transcription kit (Applied Biosystems) according to the manufacturer's instructions. For RT-PCR, all PCR conditions were the same as for genomic DNA amplification except cDNA amplified from 100 ng of RNA was used instead of DNA template.

Observation of root growth and morphology

For monitoring root growth, two independent lines from each genetic cassette were used. For each line, five propagated identical young shoots ~ 3 cm in length were subcultured in the maintenance medium under a light intensity of ~ 15 µmol/m^2/s with a 16 h/day photoperiod at 23 °C. After subculture for 6 days, the number of plants showing emergence of roots was recorded. Meanwhile, the length of its longest root among all emerged roots from each plant was measured every 24 h from day 6 to day 11. The experiment was repeated three times.

To observe the roots and root tips, a stereomicroscope with a Digital Sight DS-FI1 camera (Nikon) and NIS Elements version 3.2 software were used. About 21–29 propagated shoots per transgenic line were used and subcultured under the above conditions. After 7–9 days of subculture, when roots reached ~ 5 mm in length, only the longest root per subcultured shoot was excised and gently cleaned to remove agar for photographing. First, it was placed on a microscopic slide with a few drops of water to create

adhesion. Then it was covered with a cover slip to observe root length and root hair distribution and a picture was taken with a stereomicroscope at 1 × magnification. The measuring tool in Adobe Photoshop software (Adobe Systems) was used to measure the total root length and the length from the root hair emerging site to the root tip.

Electrophoresis and western blotting of protein extracts made from transgenic plants

Young leaves of transgenic plants grown in culture containers containing maintenance medium were harvested and ground into fine powder in liquid nitrogen. For SDS-PAGE, 150 mg each of fine powder were mixed with 350 µL of extraction buffer [50 mM Tris–HCl pH 8, 150 mM NaCl, 1% (v/v) NP40, 0.5% (w/v) sodium deoxycholate monohydrate, 0.1% (w/v) SDS, 1 mM 2-mercaptoethanol, 1 mM PMSF, 0.5 mM DTT, 1% (v/v) Sigma-Aldrich plant protease inhibitor cocktail]. After vortexing, the mixture was kept on ice for 10 min, and then subjected to two rounds of 20,000×*g* centrifugation for 10 min at 4 °C. The collected supernatant was mixed with Laemmli sample buffer and denatured at 95 °C for 5 min. The protein concentration was determined by the Bradford method. Approximately, 15 µg of proteins were separated on a 13.5% SDS-PAGE gel in running buffer containing 192 mM glycine, 25 mM Tris and 0.1% (w/v) SDS at 100 V for 70 min until the 14 kD protein marker in SeeBlue Plus2 pre-stained protein standard (Life Technologies, USA) reached the bottom end of the gel. Following separation, proteins were transferred to PVDF membrane using NuPAGE (Invitrogen) transfer buffer containing 10% (v/v) methanol and NuPAGE antioxidant. To show protein loading, the membrane was stained with 0.2% (w/v) Amido Black 10B in 10% (v/v) acetic acid and destained with H_2O.

For BN-PAGE (Invitrogen) immunoblotting, 100 mg each of fine leaf powder was mixed with 330 µL of extraction buffer containing 18 mM 3-[(3-cholamidopropyl) dimethylammonio]-1-propanesulfonic acid (CHAPS) in TBS with 10 µg/ml DNase I, 2 mM $MgCl_2$, and 1% (v/v) plant protease inhibitor cocktail (Sigma-Aldrich). After a short vortex, the mixture was incubated at 21 °C for 30 min with intermittent mixing. It was then subjected to one round of 20,000×*g* centrifugation for 20 min at 4 °C and a second round for 5 min. The collected supernatant was mixed with NativePAGE sample buffer containing 1% (w/v) Digitonin and 0.25% (w/v) Coomassie G-250. The proteins were separated on a NativePAGE (Invitrogen) 3–12% Bis–Tris gel in a NativePAGE running buffer (only cathode buffer containing 0.002% Coomassie G-250) at 100 V running into 1/3 of gel then 40 V till dye front reaching the bottom end of the gel. Following separation, proteins were transferred to PVDF membrane using NuPAGE transfer buffer at 25 V for 1 h. To visualize the unstained protein standard NativeMark (Invitrogen), the membrane was stained with 0.1% (w/v) Coomassie Brilliant Blue R-250 in 50% (v/v) methanol and destained with a solution containing 7% (v/v) acetic acid and 40% (v/v) methanol.

To detect target proteins, the membrane was blocked with 5% (w/v) BSA in PBST overnight at 4 °C and probed with anti-Huntingtin (1:1,000, ab109115, Abcam), anti-Ubiquitin (1:200, U5379, Sigma-Aldrich, USA) and biotinylated anti-Hsp70 (1:10,000, ab183437, Abcam) in blocking buffer for 1 h at 25 °C. The secondary antibody used for detecting anti-Huntingtin and anti-Ubiquitin was 1:10,000 anti-rabbit IgG conjugated with HRP. To detect biotinylated anti-Hsp70, 1:20,000 HRP-conjugated Streptavidin (1 mg/mL) was used. Luminescent signals were generated after incubation with SuperSignal® West Pico Chemiluminescent substrate (Pierce Biotechnology) and captured with Kodak Biomax X-ray film (PerkinElmer).

Filter retardation assay

Protein extracts used for BN-PAGE were diluted with 0.1% (w/v) SDS in PBS at 1:3 ratios. Samples containing 10 µg of proteins were filtered through Whatman Cellulose Acetate Membrane Filters with 0.2 µm pore sizes (GE Healthcare), which have very low protein binding capacity. Filtration was performed using an Easy-Titer® ELIFA System 77000 (Pierce Biotechnology) according to the manufacturer's instructions. After washing twice with 0.1% (w/v) SDS in PBS, the membranes were blocked with 10% (w/v) skim milk in PBST for 2 h at 25 °C. Then, the membranes were incubated with primary antibodies: 1:2000 anti-Ubiquitin and 1:20,000 anti-Huntingtin overnight at 4 °C. After washing three times with PBST, the membranes were incubated with 1:20,000 anti-rabbit IgG conjugated with HRP for 1 h at 25 °C. To detect Hsp70, the membrane was blocked with 5% (w/v) BSA in PBST and then incubated with 1:20,000 biotinylated anti-Hsp70 overnight at 4 °C, followed by 1:40,000 HRP-conjugated Streptavidin as a secondary antibody. The luminescent signals were detected as described above. To visualize the proteins, membranes were stained with 0.1% (w/v) Coomassie Brilliant Blue R-250 in 50% (v/v) methanol for 15 min and destained with a solution containing 7% (v/v) acetic acid and 40% (v/v) methanol.

Transmission electron microscopy (TEM) analysis

To observe cell structure and any aggregates in transgenic plants, TEM analysis was performed at the North Carolina State University Center for Electron Microscopy. Newly developed young leaves and roots of $Htt_{ex1}Q21$, $Htt_{ex1}Q42$, $Htt_{ex1}Q63$ and GUS transgenic plants grown in culture containers were used. Samples were cut into 1 mm^3 blocks for leaves and 0.5 mm (length) for root tips and then fixed in

3% glutaraldehyde in 0.05 M KPO_4 buffer (pH 7.0) at 4 °C. Samples were post-fixed in 2% OsO_4 in the same buffer at 4 °C in the dark. After dehydration with a graded series of ethanol, they were infiltrated and embedded with Spurr's resin (Ladd Research Industries). Samples were sectioned with a Leica UC6rt ultramicrotome (Leica Microsystems) and placed onto 200-mesh grids. The grids were then stained with 4% aqueous uranyl acetate in the dark at 25 °C followed by three distilled water washes at 40 °C and 1 min in Reynold's lead citrate followed by three more distilled water washes. All sections were observed under a JEOL JEM 1200EX transmission electron microscope (JEOL USA Inc). Images were captured using a Gatan Erlangshen Model 785 ES1000W camera and Digital Micrograph software (Gatan Inc). On average, each grid had approximately ten squares containing approximately five observable cells.

Quantitative proteomic analysis

Sample preparation for mass spectrometry analysis

Quantitative proteomic analysis was performed at the Duke Proteomics and Metabolomics Shared Resource. To prepare samples, propagated shoots from Htt_{ex1}Q21-6 and Htt_{ex1}Q63-3 lines ~ 3 cm in length were subcultured to induce roots. After 7–8 days of subculture, induced adventitious roots shorter than ~ 0.5 cm were harvested. Due to their small sizes, each sample of pooled roots with a weight of ~ 100 mg was frozen together at − 80 °C as one biological sample. Four biological samples from each line were prepared, and protein extraction was performed as follows. Harvested roots were first ground in liquid nitrogen and then resuspended in 200 µL of a buffer containing 4% (w/v) SDS and 50 mM triethylammonium bicarbonate (TEAB), pH 8.5, followed by probe sonication and heating at 80 °C for 5 min. An additional sonication step was applied. After that, the samples were centrifuged, and a BCA assay was performed on the supernatants to determine the protein concentration. Twenty-five micrograms of each sample was digested with trypsin at 1:25 (w/w) trypsin:protein using S-trap™ processing technology (Protifi). After lyophilization, peptides were reconstituted in 50 µL of 1% (v/v) trifluoroacetic acid/2% (v/v) acetonitrile (MeCN). For QC analysis, a QC pool was made by mixing equal quantities of all samples.

Quantitative mass spectrometry analysis

For quantitative mass spectrometry analysis, quantitative one-dimensional liquid chromatography coupled with tandem mass spectrometry (1D-LC–MS/MS) was performed with 2 µL of the peptide digests per sample in singlicate, including additional analyses of conditioning runs and three QC pools. The QC pooled sample was analyzed three times at the beginning and interspersed throughout the analysis of individual samples, which were alternated between the two treatment groups (Table S1). Samples were analyzed using a nanoACQUITY UPLC system (Waters) coupled to a Q-Exactive HF-X high-resolution accurate mass tandem mass spectrometer (Thermo Fisher Scientific) with a nanoelectrospray ionization source. Briefly, the sample was first trapped on a Symmetry C18 column (180 µm × 20 mm) (5 µL/min at 99.9/0.1 v/v H_2O/MeCN), followed by analytical separation using a 1.7 µm AQCUITY HSS T3 C18 column (75 µm × 250 mm) (Waters) with a 90 min gradient of 5–30% (v/v) MeCN containing 0.1% (v/v) formic acid at a flow rate of 400 nL/min and column temperature of 55 °C. Data collection on the HF-X MS was carried out in data-dependent acquisition (DDA) mode with a 120,000 resolution (@ *m*/*z* 200) full MS scan from *m*/*z* 375 to 1600 with a target AGC value of 3e6 ions and 50 ms maximum injection time (IT). The top 30 peptides were selected for MS/MS using a resolution of 15,000, max AGC of 5e4 ions and minimum AGC target of 2.25e3, max IT of 45 ms, collision energy of 27, an isolation width of 1.2 *m*/*z* and 20 s dynamic exclusion. The total analysis cycle time for each sample injection was approximately 2 h.

Protein identification and quantitation

Following UPLC-MS/MS analyses, data were imported into Rosetta Elucidator v4.0 (Rosetta Biosoftware Inc), and analyses were aligned based on the accurate mass and retention time of detected ions ("features") using the PeakTeller algorithm. Relative peptide abundance was computed based on the area-under-the-curve of the selected ion chromatograms of the aligned features across all runs. The MS/MS data were searched against a custom Swiss-Prot/TrEMBL database with *N. tabacum* taxonomy (downloaded on 04/30/2018). To minimize sequence redundancy, the database was further curated using cd-hit (http://weizhongli-lab.org/cdhit_suite/cgi-bin/index.cgi?cmd=cd-hita) with a sequence identity cutoff of 0.9, and an equal number of reverse entries was added for decoy database searching. The final database had 90,193 total entries. Mascot Distiller and Mascot Server (v 2.5, Matrix Sciences) were employed to produce fragment ion spectra and to perform the database searches. The parameters used for the database search included a precursor mass tolerance of 5 ppm, a production mass tolerance of 0.02 Da, trypsin specificity with up to 2 missed cleavages, fixed modification on Cys (carbamidomethyl) and variable modification of N-terminal protein acetylation. Individual peptide was scored using the PeptideProphet algorithm in Rosetta Elucidator, and data were annotated at a 1.0% peptide false discovery rate. For quantitative analysis, the data were first curated to contain only high-quality peptides with appropriate chromatographic peak shapes and the dataset

was intensity scaled to the robust median across all samples. To analyze abundance, the expression values of these 5073 proteins quantified by 2 or more peptides were *Z*-score-normalized followed by 2D hierarchical clustering analysis in Rosetta Elucidator.

Meanwhile, both analytical variability and biological variability were analyzed to determine the quality of quantitative proteomic analysis. To assess technical reproducibility, the percentage (%) of coefficient of variation (CV) was calculated for each protein across the three injections of a QC pool that were interspersed throughout the study, while %CVs were also measured for each protein across the individual analyses to assess biological variability.

GO enrichment and heatmap visualization analyses

DAPs (1693 total with 854 abundance-increased and 839 abundance-decreased) with abundance changes more than 1.5-fold were subjected to GO enrichment analysis using the AgriGO platform v2.0 webserver (http://systemsbiology.cau.edu.cn/agriGOv2/) [70]. The UniProt batch retrieval tool (http://www.uniprot.org/uploadlists) was used to map proteins to tobacco (*N. tabacum*, cv. TN90) proteome (ID: UP000084051) to obtain UniProtKB for GO term identification. Of the 73,605 proteins of the tobacco proteome, 49,741 had GO annotation. Among 1693 DAPs, 1366 had GO annotation. To expand the GO annotation of the remaining 327 DAPs, these protein sequences were further used to query the uniprot_proteome (ID: AUP000004994) of *Solanum lycopersicum* (Tomato) (Strain: cv. Heinz 1706) using the BLASTP program with an E-value ≤ 1e−5 and identity ≥ 40% as the cutoff. The results added GO annotation for additional 122 proteins, whereas 205 proteins remained unannotated. Overall, the GO annotation of 745 (698 from tobacco, 47 from tomato) abundance-increased proteins and 743 (668 from tobacco, 75 from tomato) abundance-decreased proteins were included in the GO enrichment analysis. The GO terms of the abundance-increased or abundance-decreased proteins were imported separately into AgriGO for GO enrichment analysis. AgriGO's Singular Enrichment Analysis (SEA) was used to identify enriched GO with default settings [Statistical test method: Fisher, Multi-test adjustment method: Yekutieli (FDR under dependency), Significance Level: 0.05, Minimum number of mapping entries: 5, and Gene ontology type: complete GO]. Selected enriched GO terms with biological importance were presented by GO Enrichment Plot (EHBIO gene technology).

To show the increased or decreased levels of DAPs associated with root growth and the maintenance of root apex structure, a heatmap visualization analysis was performed using Heml version 1.0.1 software [71]. The value assigned to each protein in $Htt_{ex1}Q21$ and $Htt_{ex1}Q63$ was calculated first as the expression ratio by comparing the relative abundance of any individual protein with its average of the two treatment groups, and then subjected to log2 transformation as described [72].

Animals

All procedures for using animals in the experiments were carried out in accordance with the National Institutes of Health 'Guide for Care and Use of Laboratory Animals' and were approved by the Institutional Animal Care and Use Committee of North Carolina Central University. Three-week-old R6/2 (B6CBA-Tg(HDexon1)62Gpb/125J) HD mice expressing Htt_{ex1} carrying approximately 120 ± 5 (CAG) repeats and 3-week-old wild-type B6CBA-Nocarrier mice (NCAR) were purchased from the Jackson Laboratory (Bar Harbor). The animal housing room had a controlled temperature of 20 ± 2 °C, humidity of 40–60%, and a 12-h light/12-h dark cycle. Animals had free access to food (Rodent Diet 20, PicoLab) and water. Both types of mice at 4 weeks of age were used first to collect blood for metabolite analysis and then sacrified to harvest the brains for western blotting, histopathology and immunohistochemistry.

Electrophoresis and western blotting of protein extracts from brain tissues

To isolate proteins from total brain tissues ($n = 7$), whole brain frozen in liquid nitrogen and stored at − 80 °C freezer was used. The tissues were individually homogenized with N-PER™ Neuronal Protein Extraction Reagent (Cat. #: 87792, Thermo Fisher Scientific) containing Halt Protease and Phosphatase Inhibitor Cocktail (Thermo Fisher Scientific). Protein concentrations of the samples were measured using a BCA Protein Assay kit (Thermo Fisher Scientific). An equal amount of protein (25 µg) was loaded into each lane, separated on 4–12% Bis–Tris NuPAGE gels (Invitrogen, Carlsbad, CA, USA) and transferred to PVDF membranes (MilliporeSigma) using an XCell SureLock mini-cell system (Invitrogen). After transfer, membranes were blocked with Li-COR Odyssey Blocking buffer (Li-COR Biosciences). The membranes were subsequently probed with the following primary antibodies. Gamma-tubulin was used as an internal control. Anti-Htt (clone mEM48, MAB5374) and anti-γ-tubulin (T6557) antibodies were obtained from Sigma-Aldrich. Anti-GCH-1 (A305-296A-M-1) was obtained from Bethyl Laboratories. Anti-DHFR (ab124814)), anti-TPH2 (ab184505), anti-QDPR/DHPR polyclonal (ab126150), and anti-MTHFR (ab203786) antibodies were obtained from Abcam. Anti-MS (68796), anti-TH (58844S), anti-ChAT (27269) and anti-nNOS (4234) antibodies were purchased from Cell Signaling Technology. Anti-MAT1/2A (NB110-94162) and anti-AHCY

(NBP1-55016) antibodies were purchased from Novus Biologicals. Following incubation with primary antibodies, the membranes were probed with IRDye 680RD conjugated to Goat anti-Rabbit IgG or IRDye 800CW conjugated to Goat-anti-Mouse IgG secondary antibody (1:10,000 dilution, LI-COR Biosciences). Image acquisition was performed with a LI-COR Odyssey Infrared Fluorescent scanner (LI-COR Biosciences). Western blot images were recorded into "tif" picture file and "black to white and white to black" under the software was chose. All protein bands were quantified using LI-COR software and are expressed as the ratio of each targeted protein band fluorescence intensity to that of γ-tubulin.

Crystal violet staining

All mice were anesthetized, and their brains were removed and post-fixed in 4% PBS-buffered paraformaldehyde for 24 h. The brain was embedded in paraffin, and a series of consecutive coronal sections (4 µm in thickness) were prepared using the same protocols as described [73] for crystal violet staining and immunohistochemistry assays. For crystal violet staining, the sections were submerged in graded ethanol and xylene vitrification for demyelination. The sections were stained with 0.1% cresyl violet for 1 min, washed with distilled water, dehydrated with graded ethanol for vitrification, and finally coverslipped. Striatal volumes were calculated using Cavalieri's principle (volume $= s_1d_1 + s_2d_2 + \cdots + s_nd_n$, where s is the surface area and d is the distance between two sections).

Immunohistochemistry (IHC) assay

For the immunohistochemistry assay, the prepared sections were submerged in citrate buffer (pH 6.0) and heated at boiling temperature in a pressure cooker for 10 min for antigen retrieval. The expression level of Htt, GTPCH and DHFR proteins were examined in each group after incubation with primary antibody overnight and HRP-conjugated secondary antibody incubation at 37 °C for 45 min. The reaction was visualized with a Pierce™ DAB Substrate Kit (Thermo Fisher Scientific) followed by hematoxylin staining (Abcam) of the nuclei. The number of positively stained cells was counted in five randomly selected microscopic fields at 400 ×. The average of stained cells was calculated.

BH_4 and BH_2 measurements

To measure BH_4 and BH_2 in the plasma of R6/2 and NCAR mice ($n = 4$), blood (~ 1 mL) from each mouse was collected by cardiac puncture into an EDTA-coated tube containing 100 µL of 1% freshly prepared DTT stock solution to give a final DTT concentration of 0.1% to protect BH_4 from oxidation as described by Fekkes and Voskuilen-Kooijman [74]. Collected blood was centrifuged at 2000×*g* for 15 min to isolate plasma within 30 min after collection. Plasma was stored at − 80 °C. To analyze BH_4 and BH_2 in the brain ($n = 4$), brain tissues were first ground with liquid nitrogen. Subsequent sample preparation and LC–MS/MS analysis to measure BH_4 and BH_2 levels in both plasma and brain tissues were performed as described by Shen et al. [75].

Amino acid measurements

To measure the contents of amino acids in the plasma of R6/2 and NCAR mice ($n = 4$), blood from each mouse was collected by cardiac puncture into an EDTA-coated tube. Collected blood was centrifuged at 2000×*g* for 15 min to isolate plasma within 30 min after collection. Collected plasma was stored at – 80 °C until analysis. To analyze the contents of amino acids in the brain ($n = 4$), the brain was excised after anesthetization. Then brain tissues were ground in liquid nitrogen. For detecting amino acids in plasma and brain tissues, the same protocols for sample preparation and Ultraperformance® Liquid Chromatography (UPLC) analysis as described by Peake et al. [76] were used.

Statistical analysis

For all the experiments except the proteomic analysis, the obtained results are presented as the average ± SD. Statistical significance was analyzed using one-way ANOVA and Student's *t* tests for pairwise mean comparisons ($p < 0.05$). For proteomic analysis, we calculated fold-changes as log2-ratio between average values of $Htt_{ex1}Q63$ vs. $Htt_{ex1}Q21$ groups and performed Student's *t* test with and without Benjamini–Hochberg correction for multiple hypothesis testing.

Supplementary Information The online version contains supplementary material available at https://doi.org/10.1007/s00018-022-04587-6.

Acknowledgements We thank Dr. M.W. Foster and Dr. M.A. Moseley for the proteomic analysis, Ms. V.M. Knowlton for the help with TEM, Dr. W.Z. Duan for discussions and critical reading of the manuscript, Dr. Y.-H. Sun for helpful discussions in GO analysis, and Dr. S.H. Li for providing PCR buffer information.

Author contributions TD and JX designed the research; C-YH, CSZ, FSK, MTH, EA, GSJ, MDT, TD, and JX performed the experiments; C-YH, FSK, EA, TD and JX analyzed the data. C-YH, FSK and JX drafted the manuscript with input from all the authors.

Funding This work was supported by grants from the National Institute of General Medical Sciences (SC1GM111178) to J.X. and a scholarship from the China Scholarship Council (201306305041) to C.S.Z.

Availability of data and materials The datasets of quantitative proteomic analysis generated for this study were uploaded to MassIVE, and were assigned the dataset identifier MassIVE MSV000084557, which can be accessed at ftp://MSV000084557@massive.ucsd.edu using password 4981 and will be made publicly available once the

paper is published. All other data, materials and methods are available from the corresponding authors upon request.

Declarations

Conflict of interests The authors declare no conflict of interest.

Ethics approval and consent to participate All the procedures for using animals in the experiments were carried out in accordance with the National Institutes of Health 'Guide for Care and Use of Laboratory Animals' and were approved by the Institutional Animal Care and Use Committee of North Carolina Central University.

Consent for publication All the authors participated in this study checked the manuscript and agreed with this publication.

References

1. Naphade S, Tshilenge KT, Ellerby LM (2019) Modeling polyglutamine expansion diseases with induced pluripotent stem cells. Neurotherapeutics 16:979–998
2. Di Prospero NA, Fischbeck KH (2005) Therapeutics development for triplet repeat expansion diseases. Nat Rev Genet 6:756–765
3. The Huntington's Disease Collaborative Research Group (1993) A novel gene containing a trinucleotide repeat that is expanded and unstable on Huntington's disease chromosomes. Cell 72:971–983
4. Veldman MB, Yang XW (2018) Molecular insights into cortico-striatal miscommunications in Huntington's disease. Curr Opin Neurobiol 48:79–89
5. Genetic Modifiers of Huntington's Disease (GeM-HD) Consortium (2019) CAG repeat not polyglutamine length determines timing of Huntington's disease onset. Cell 178:887-900.e14
6. Wertz MH et al (2020) Genome-wide in vivo CNS screening identifies genes that modify CNS neuronal survival and mHTT toxicity. Neuron 106:76–89 (**e8**)
7. Brenner ED et al (2006) Plant neurobiology: an integrated view of plant signaling. Trends Plant Sci 11:413–419
8. Baluska F (2010) Recent surprising similarities between plant cells and neurons. Plant Signal Behav 5:87–89
9. Guttman DC (2004) Plants as models for the study of human pathogenesis. Biotechnol Adv 22:363–382
10. Spampinato CP, Gomez-Casati DF (2012) Research on plants for understanding of disease of nuclear and mitochondrial origin. J Biomed Biotechnol 2012:836196
11. Hanson AD, Gage DA, Shachar-Hill Y (2000) Plant one-carbon metabolism and its engineering. Trends Plant Sci 5:206–213
12. Gorelova V, Ambach L, Rébeillé F, Stove C, Van Der Straeten D (2017) Folates in plants: research advances and progress in crop biofortification. Front Chem 5:21
13. Coppedè F (2010) One-carbon metabolism and Alzheimer's disease: focus on epigenetics. Curr Genom 11:246–260
14. Thomas EA (2016) DNA methylation in Huntington's disease: Implications for transgenerational effects. Neurosci Lett 625:34–39
15. Ducker GS, Rabinowitz JD (2017) One-carbon metabolism in health and disease. Cell Metab 25:27–42
16. Mohd Murshid N, Aminullah Lubis F, Makpol S (2022) Epigenetic changes and its intervention in age-related neurodegenerative diseases. Cell Mol Neurobiol 42:577–595
17. Kapatos G (2013) The neurobiology of tetrahydrobiopterin biosynthesis: a model for regulation of GTP cyclohydrolase I gene transcription within nigrostriatal dopamine neurons. IUBMB Life 65:323–333
18. Pouladi MA, Morton AJ, Hayden MR (2013) Choosing an animal model for the study of Huntington's disease. Nat Rev Neurosci 14:708–721
19. Chang R, Liu X, Li SH, Li XJ (2015) Transgenic animal models for study of the pathogenesis of Huntington's disease and therapy. Drug Des Dev Ther 9:2179–2188
20. Li SH, Li XJ (1998) Aggregation of N-terminal huntingtin is dependent on the length of its glutamine repeats. Hum Mol Genet 7:777–782
21. Vonsattel JP, DiFiglia M (1998) Huntington disease. J Neuropathol Exp Neurol 57:369–384
22. Landles C, Bates GP (2004) Huntingtin and the molecular pathogenesis of Huntington's disease. Fourth in molecular medicine review series. EMBO Rep 5:958–963
23. Kim YE et al (2016) Soluble oligomers of polyQ-expanded huntingtin target a multiplicity of key cellular factors. Mol Cell 63:951–964
24. Hu J et al (2009) A class of dynamin-like GTPases involved in the generation of the tubular ER network. Cell 138:549–561
25. Chen J, Stefano G, Brandizzi F, Zheng H (2011) Arabidopsis RHD3 mediates the generation of the tubular ER network and is required for Golgi distribution and motility in plant cells. J Cell Sci 124:2241–2252
26. Lee H et al (2013) An Arabidopsis reticulon and the atlastin homologue RHD3-like2 act together in shaping the tubular endoplasmic reticulum. New Phytol 197:481–489
27. Oláh J et al (2008) Increased glucose metabolism and ATP level in brain tissue of Huntington's disease transgenic mice. FEBS J 275:4740–4755
28. Bossy-Wetzel E, Petrilli A, Knott AB (2008) Mutant huntingtin and mitochondrial dysfunction. Trends Neurosci 31:609–616
29. Hosp F et al (2017) Spatiotemporal proteomic profiling of Huntington's disease inclusions reveals widespread loss of protein function. Cell Rep 21:2291–2303
30. Libault M, Brechenmacher L, Cheng J, Xu D, Stacey G (2010) Root hair systems biology. Trends Plant Sci 15:641–650
31. Balcerowicz D, Schoenaers S, Vissenberg K (2015) Cell fate determination and the switch from diffuse growth to planar polarity in Arabidopsis root epidermal cells. Front Plant Sci 6:1163
32. Mencacci NE et al (2014) Parkinson's disease in GTP cyclohydrolase 1 mutation carriers. Brain 137:2480–2492
33. Raychaudhuri S, Sinha M, Mukhopadhyay D, Bhattacharyya NP (2008) HYPK, a Huntingtin interacting protein, reduces aggregates and apoptosis induced by N-terminal Huntingtin with 40 glutamines in Neuro2a cells and exhibits chaperone-like activity. Hum Mol Genet 17:240–255
34. Wang H, Lockwood SK, Hoeltzel MF, Schiedelbein JW (1997) The ROOT HAIR DEFECTIVE3 gene encodes an evolutionarily conserved protein with GTP-binding motifs and is required for regulated cell enlargement in Arabidopsis. Genes Dev 11:799–811

35. Aberg K, Saetre P, Jareborg N, Jazin E (2006) Human QKI, a potential regulator of mRNA expression of human oligodendrocyte-related genes involved in schizophrenia. Proc Natl Acad Sci USA 103:7482–7487
36. Forde BG, Lea PJ (2007) Glutamate in plants: metabolism, regulation, and signaling. J Exp Bot 58:2339–2358
37. Basset G et al (2002) Folate synthesis in plants: the first step of the pterin branch is mediated by a unique bimodular GTP cyclohydrolase I. Proc Natl Acad Sci USA 99:12489–12494
38. Hersch SM, Ferrante RJ (2004) Translating therapies for Huntington's disease from genetic animal models to clinical trials. NeuroRx 1:298–306
39. Kurian MA, Gissen P, Smith M, Heales S Jr, Clayton PT (2011) The monoamine neurotransmitter disorders: an expanding range of neurological syndromes. Lancet Neurol 10:721–733
40. Xu F et al (2014) Disturbed biopterin and folate metabolism in the Qdpr-deficient mouse. FEBS Lett 588:3924–3931
41. Luo M, Piffanelli P, Rastelli L, Cella R (1993) Molecular cloning and analysis of a cDNA coding for the bifunctional dihydrofolate reductase-thymidylate synthase of *Daucus carota*. Plant Mol Biol 22:427–435
42. Rangel-Barajas C, Rebec GV (2016) Dysregulation of corticostriatal connectivity in Huntington's disease: a role for dopamine modulation. J Huntingtons Dis 5:303–331
43. Fanet H et al (2020) Tetrahydrobiopterin administration facilitates amphetamine-induced dopamine release and motivation in mice. Behav Brain Res 379:112348
44. Newman AC, Maddocks ODK (2017) One-carbon metabolism in cancer. Br J Cancer 116:1499–1504
45. Reina-Campos M, Diaz-Meco MT, Moscat J (2020) The complexity of the serine glycine one-carbon pathway in cancer. J Cell Biol 219:e201907022
46. Berry MD (2004) Mammalian central nervous system trace amines. Pharmacologic amphetamines, physiologic neuromodulators. J Neurochem 90:257–271
47. Pei Y, Asif-Malik A, Canales JJ (2016) Trace amines and the trace amine-associated receptor 1: pharmacology, neurochemistry, and clinical implications. Front Neurosci 10:148
48. Albrecht J, Sidoryk-Węgrzynowicz M, Zielińska M, Aschner M (2011) Roles of glutamine in neurotransmission. Neuron Glia Biol 6:263–276
49. Zielińska M, Ruszkiewicz J, Hilgier W, Fręśko I, Albrecht J (2011) Hyperammonemia increases the expression and activity of the glutamine/arginine transporter y+ LAT2 in rat cerebral cortex: implications for the nitric oxide/cGMP pathway. Neurochem Int 58:190–195
50. Emery PW (2013) Amino acids: metabolism. In: Caballero B (ed) Encyclopedia of human nutrition, 3rd edn. Academic Press, Cambridge, pp 72–78
51. Walters DC et al (2019) Metabolomic analyses of vigabatrin (VGB)-treated mice: GABA-transaminase inhibition significantly alters amino acid profiles in murine neural and non-neural tissues. Neurochem Int 125:151–162
52. Mochel F et al (2007) Early energy deficit in Huntington disease: identification of a plasma biomarker traceable during disease progression. PLoS One 2:e647
53. Mochel F, Benaich S, Rabier D, Durr A (2011) Validation of plasma branched chain amino acids as biomarkers in Huntington disease. Arch Neurol 68:265–267
54. Skene DJ et al (2017) Metabolic profiling of presymptomatic Huntington's disease sheep reveals novel biomarkers. Sci Rep 7:43030
55. Wu G (2009) Amino acids: metabolism, functions, and nutrition. Amino Acids 37:1–17
56. Moss DJH et al (2017) Identification of genetic variants associated with Huntington's disease progression: a genome-wide association study. Lancet Neurol 16:701–711
57. Jiang X et al (2019) A novel GTPCH deficiency mouse model exhibiting tetrahydrobiopterin-related metabolic disturbance and infancy-onset motor impairments. Metabolism 94:96–104
58. Glajch KE, Sadri-Vakili G (2015) Epigenetic mechanisms involved in Huntington's disease pathogenesis. J Huntingtons Dis 4:1–15
59. Sharma S, Taliyan R (2015) Transcriptional dysregulation in Huntington's disease: the role of histone deacetylases. Pharmacol Res 100:157–169
60. Lee J, Hwang YJ, Ryu H, Kowall NW, Ryu H (2014) Nucleolar dysfunction in Huntington's disease. Biochim Biophys Acta 1842:785–790
61. Raymond LA et al (2011) Pathophysiology of Huntington's disease: time-dependent alterations in synaptic and receptor function. Neuroscience 198:252–273
62. Moreno-Jiménez EP et al (2019) Adult hippocampal neurogenesis is abundant in neurologically healthy subjects and drops sharply in patients with Alzheimer's disease. Nat Med 25:554–560
63. Musa TA, Hung C-Y, Darlington DE, Sane DC, Xie JH (2009) Overexpression of human erythropoietin in tobacco does not affect plant fertility or morphology. Plant Biotechnol Rep 3:157–165
64. Holsters M et al (1978) Transfection and transformation of *Agrobacterium tumefaciens*. Mol Gen Genet 163:181–187
65. Twyman RM, Stoger E, Schillberg S, Christou P, Fischer R (2003) Molecular farming in plants: host systems and expression technology. Trends Biotechnol 21:570–578
66. Dewey RE, Xie JH (2013) Molecular genetics of alkaloid biosynthesis in *Nicotiana tabacum*. Phytochemistry 94:10–27
67. Horsch RB et al (1988) Leaf disc transformation. In: Gelvin SB, Schilperoot RA, Verma DPS (eds) Plant molecular biology manual, Kluwer Academic, pp 63–71
68. Jama M, Millson A, Miller CE, Lyon E (2013) Triplet repeat primed PCR simplifies testing for Huntington disease. J Mol Diagn 15:255–262
69. Huang B et al (2015) Mutant huntingtin down-regulates myelin regulatory factor-mediated myelin gene expression and affects mature oligodendrocytes. Neuron 85:1212–1226
70. Tian T et al (2017) AgriGO v2.0: a GO analysis toolkit for the agricultural community, 2017 update. Nucleic Acids Res 45(W):W122–W129
71. Deng W, Wang Y, Liu Z, Cheng H, Xue Y (2014) HemI: a toolkit for illustrating heatmaps. PLoS One 9:e111988
72. Babu MM (2004) An introduction to microarray data analysis. In: Grant RP (ed) Computational Genomics: Theory and Application, Horizon Bioscience, pp 225–249
73. Mehta SL, Kumari S, Mendelev N, Li PA (2012) Selenium preserves mitochondrial function, stimulates mitochondrial biogenesis, and reduces infarct volume after focal cerebral ischemia. BMC Neurosci 13:79
74. Fekkes D, Voskuilen-Kooijman A (2007) Quantitation of total biopterin and tetrahydrobiopterin in plasma. Clin Biochem 40:411–413
75. Shen JS et al (2017) Tetrahydrobiopterin deficiency in the pathogenesis of Fabry disease. Hum Mol Genet 26:1182–1192
76. Peake RWA et al (2013) Improved separation and analysis of plasma amino acids by modification of the MassTrak™ AAA Solution Ultraperformance® liquid chromatography method. Clin Chim Acta 423:75–82